Full title: Conjunctive spatial and idiothetic codes are topographically organized in the GABAergic cells of the lateral septum

Authors: Suzanne van der Veldt[1], Guillaume Etter[1], Fernanda Sosa[1], Coralie-Anne Mosser[1], Sylvain Williams[1*]

[1] McGill University & Douglas Mental Health University Institute, Montreal, Canada
6875, Boul. LaSalle, Verdun (Quebec), H4H 1R3, Phone: 514 761-6131, Fax: 514 888-4067
*Corresponding author: sylvain.williams@mcgill.ca

Author contributions

SV and SW designed the study. SV performed surgeries, behavioral recording experiments, immunohistological experiments, and calcium data analysis. GE wrote code for MI calculation and Bayesian decoding and implanted mice for CA1 recordings. FS assisted with behavioral recording experiments, immunohistological experiments and performed quantifications. CAM implanted two mice that were used in the current study. SV and SW wrote the manuscript with inputs from all authors.

Abstract

The hippocampal spatial code's relevance for downstream neuronal populations – particularly its main subcortical output, the lateral septum (LS) - is still poorly understood. Here, using calcium imaging combined with unbiased analytical methods, we functionally characterized and compared the spatial tuning of LS GABAergic cells to those of dorsal CA3 and CA1 cells. We identified a significant number of LS cells that are modulated by place, speed, acceleration, and direction, as well as conjunctions of these properties, directly comparable to

hippocampal CA1 and CA3 place cells. Interestingly, Bayesian decoding of position based on LS place cells reflected the animal's location as accurately as decoding using the activity of hippocampal pyramidal cells. A portion of LS place cells showed stable fields over the course of multiple days, potentially reflecting long-term episodic memory. The distributions of cells exhibiting these properties formed gradients along the anterior-posterior and dorsal-ventral axes of the LS, directly reflecting the organization of hippocampal inputs to the LS. Finally, we show using trans-synaptic tracing that LS neurons receiving CA3 and CA1 excitatory input send projections to the hypothalamus and medial septum, regions that are not targeted directly by principal cells of the dorsal hippocampus. Together, our findings demonstrate that the LS accurately and robustly represents spatial and idiothetic information and is uniquely positioned to relay this information from the hippocampus to its downstream regions, thus occupying a key position within a distributed spatial memory network.

Introduction

The lateral septum (LS) is an anatomically complex structure uniquely positioned within a broader distributed spatial memory network. The LS consists almost exclusively of highly interconnected inhibitory GABAergic cells (Zhao et al., 2013) that are densely innervated by the principal cells of the hippocampus (Risold and Swanson, 1996; Tingley and Buzsáki, 2018). Previous research has implicated the LS in a wide variety of behaviors, including spatial and working memory (Brito and Thomas, 1981; Rawlins and Olton, 1982; Stanton et al., 1984; Thomas, 1979; Thomas and Brito, 1980), the regulation of feeding (Calderwood et al., 2020; Carus-Cadavieco et al., 2017; Sweeney and Yang, 2016; Xu et al., 2019), anxiety (Anthony et al., 2014; Besnard et al., 2019; Sparks and Ledoux, 2000; Trent and Menard, 2010), locomotion (Bender et al., 2015; Wirtshafter and Wilson, 2019), and

social behaviors (Bredewold et al., 2015; Chee et al., 2015; Clemens et al., 2020; Leroy et al., 2018).

To date, functional characterizations of the LS have often focused on the spatial coding properties of these neurons, primarily due to the extensive excitatory input from positionally-tuned hippocampal pyramidal neurons, commonly referred to as 'place cells' (Leroy et al., 2018; Risold and Swanson, 1997; Swanson and Cowan, 1977; Tingley and Buzsáki, 2018). Yet, this body of work has not yet yielded a consensus. Several studies have reported place cells in the LS, but the number, information content, and stability vary widely from study to study (Kita et al., 1995; Leutgeb and Mizumori, 2002; Nishijo et al., 1997; Takamura et al., 2006; Wirtshafter and Wilson, 2019; Zhou et al., 1999), while others described a lack of canonical place cells (Tingley and Buzsáki, 2018). As previous studies often depended on variable criteria of what defines a place cell, estimates range from 5.3% (Tingley and Buzsáki, 2018) to 56.0% (Wirtshafter and Wilson, 2019) of LS cells classified as spatially-modulated. Strikingly, even estimates by the same authors on data acquired from the same subjects engaging the same task ranged between 26.5% (Wirtshafter and Wilson, 2020) to 56.0% (Wirtshafter and Wilson, 2019). When reported, LS place cells are typically described as of lesser quality than classic hippocampal place cells, with lower within-session stability and larger place fields (Takamura et al., 2006; Zhou et al., 1999). Adding to this complexity, the LS is a large structure that is cytoarchitecturally subdivided into dorsal, intermediate, and ventral subregions spread across its anterior-posterior axis (Risold and Swanson, 1997; Swanson and Cowan, 1977), suggesting that, in addition to subjective criterias, the striking differences in LS spatial coding characteristics between studies may be in part a product of variations in recording locations within the region. In addition to positional information, LS neurons may also encode idiothetic information, such as

acceleration, velocity, and direction (Takamura et al., 2006; Wirtshafter and Wilson, 2019; Zhou et al., 1999).

Beyond their spatial tuning properties, hippocampal place cells are also noted for the rapid reorganization of the place fields across time (on the order of days) and navigational contexts, a phenomenon termed remapping (Gonzalez et al., 2019; Howard and Kahana, 2002; Mankin et al., 2015; Rubin et al., 2015; Ziv et al., 2013). If the LS spatial code is directly inherited from its hippocampal inputs, one would expect comparable dynamics over a similar timescale. In contrast, the LS has been implicated in behaviors that may require a stable representation of space over time, including context-reward (Luo et al., 2011a; McGlinchey and Aston-Jones, 2018), contextual fear conditioning (Besnard et al., 2019; Butler et al., 2015; Garcia et al., 1997; Reis et al., 2010; Vetere et al., 2017) and spatial learning and memory (Leutgeb and Mizumori, 1999; M'Harzi and Jarrard, 1992; Wirtshafter and Wilson, 2020). Thus, whether and how the LS spatial code changes across time is crucial to clarifying its relationship to the upstream hippocampal spatial code, with important implications for its involvement in this broader spatial memory network and how it supports behaviors across longer timescales.

To resolve these outstanding questions, we functionally characterize hippocampal connectivity of LS, and asked how information rich LS neurons are in relation to their main hippocampal inputs dorsal CA3 and CA1. To this end, we used head-mounted miniaturized microscopes to record ~2000 LS neurons across the anterior-posterior and dorsal-ventral axes of the LS, and compared their firing characteristics to pyramidal cells recorded in CA1 and CA3, as animals navigated linear track and open field environments. Results demonstrate that the LS accurately and robustly represents spatial, speed, and directional information in an anatomically-organized fashion. While the information of LS neurons is generally comparable to CA3 and CA1, our tracing studies suggest that LS information is sent to

downstream brain regions such as the medial septum and hypothalamus that are not directly connected by the principal cells of the dorsal hippocampus.

Results

LS GABAergic neurons exhibit stable spatial activity during alternation in linear track

Previous electrophysiological studies of the lateral septum disagree on both the proportion of place encoding cells in this region and their spatial content. Cells have been previously described to be of lower quality than the classically described hippocampal place cells (Takamura et al., 2006; Wirtshafter et al., 2019; 2020) or to be virtually absent (Tingley & Buzsaki, 2018).

First, to assess the distribution of excitatory pyramidal inputs from each hippocampal subregion to the GABAergic cells of the LS, we injected a monosynaptic retrograde rabies tracer in dorsal LS (Figure 1A, Supplemental figure 1, n = 5 mice). We observed strong labeling of pyramidal neurons of the hippocampus in area CA1 and CA3 (Figure 1B, Supplemental figure 1). To investigate how the spatial coding properties of the LS compare to these main dorsal hippocampal inputs, we expressed the calcium (Ca^{2+}) indicator GCaMP6f in the GABAergic cells of the LS or in the pyramidal cells of the dorsal CA1 (dCA1) and dorsal CA3 (dCA3) of mice (Figure 1C). We recorded Ca^{2+} activity of 1082 LS neurons (N = 15 mice), 1148 dCA1 pyramidal cells (N = 5 mice) and 144 cells from dCA3 (N = 2 mice) from animals alternating on a linear track. We subsequently filtered and binarized the recorded calcium traces (Supplemental figure 2A, Etter et al., 2020) and excluded periods of immobility ($< 5 cm.s^{-1}$). Using an information-theoretic framework (Shannon, 1948; Skaggs et al., 1993; Souza et al., 2018), we computed the mutual information (MI) between calcium activity and spatial location for each cell and expressed

the results in bits (30 bootstrap samples, 50% data sampling, Supplemental figure 2B-C, Etter et al., 2020). We found that LS GABAergic activity was significantly spatially modulated in comparison to circularly shuffled surrogates ($p < .01$, Figure 1D, Supplemental figure 2C, H). Indeed, both mutual information and within-session stability was higher for spatially modulated LS cells than for non-modulated (Wilcoxon test, $p < .0001$, Supplemental figure 1E,F). Using this approach, a total of 43.90% of LS GABAergic cells qualified as place cells (475/1082 cells), as compared to 31.05% in CA1 (336/1148 cells) and 32.63% in CA3 (47 cells/144 cells), with LS cells similarly distributed along the linear track as classical hippocampal place cells (Figure 1E). In contrast to previous reports (Tingley & Buzsaki, 2018; Wirtshafter & Wilson, 2019, 2020), we thus observed a significantly higher proportion of place cells in LS as compared to CA1 and CA3 (Kruskall-Wallis, $H(3) = 6.102$, $p = .0298$, Figure 1F). We found that even though within-session stability of place cells was significantly different between LS, dCA1, and dCA3, stability in the LS was not significantly different than in dorsal CA1 (Kruskall-Wallis, $H(3) = 8.922$, $p = .0116$, Figure 1G).

In contrast to their omnidirectional firing properties in open field environments, hippocampal neurons rapidly develop strong directional selectivity in linear tracks (Markus et al., 1995; McNaughton et al., 1983; Navratilova et al., 2012). To test whether the LS place code developed comparable directional selectivity, we ranked place cells as a function of the difference between left and right MI (Supplemental figure 3A-D), we found LS cells tuned to the absolute location regardless of direction (83/1082, 7.67%), while other cells were selective to the left- (168/1082, 15.52%), or right-trajectories (239/1082, 22.08%).

Previous studies have used decoding methods to predict behavioral variables from calcium imaging data recorded in the hippocampus (Gonzalez et al., 2019; Mau et al., 2018; Ziv et al., 2013), yielding insights into the amount of information encoded by a neuronal assembly. Here, we asked whether we could reliably estimate the mouse location solely from

LS neuronal activity patterns. To assess decoding accuracy and make sure our Bayesian decoder worked well, we computed the mean decoding error and mean decoding accuracy (Figure 1H-J, see methods) for CA1. Indeed, using a bootstrapped sample of 60 cells, a decoder using CA1 calcium data significantly outperformed a decoder that was trained using shuffled data (paired t-test, $t(4) = 7.558$, $p = .0016$, Figure 1K). Decoding location using LS neuronal activity significantly outperformed a decoder that was trained using shuffled data (paired t-test, $t(6) = 13.56$, $p < .0001$, Figure 1K), even when decreasing the number of neurons used, for both decoding error (two-way RM ANOVA, $F(3,19) = 571.4$, $p = 0.0024$ for main effect of shuffle, $F(3,19) = 6.948$, $p = 0.0024$ for main effect of number of included cells; Supplemental figure 4A) and decoding agreement (two-way RM ANOVA, $F(3,19) = 1059$, $p < .0001$ for main effect of shuffle, $F(3,19) = 10.06$, $p = 0.0003$ for main effect of number of included cells; Supplemental figure 3A). A decoder trained using CA3 data was not significantly different from shuffle ($t(1) = 2.597$, $p = .2305$), which is likely due to the low number of animals included in the analysis. In order to compare decoding accuracy for LS, CA1 and CA3, a decoding score was computed (Figure 1L, see methods), and we found that LS significantly outperforms CA3 (one-way ANOVA, $F(2,11) = 7.662$, $p = .0082$). Overall, place cells recorded in LS were significantly more active than those recorded in the hippocampus ($H(3) = 155.1$, $p < .0001$, Supplemental figure 2G), which could contribute to the overall higher decoding accuracy using LS cells.

LS GABAergic neurons exhibit stable spatial activity during free exploration in a 2D environment

In order to assess spatial coding during free exploration in a two-dimensional environment, we recorded Ca2+ activity of 1889 neurons in 28 mice implanted in distinct subregions of the LS, while the animals were freely exploring a novel open field. Out of 1889 recorded cells,

38.01% (718/1889, N = 28) of LS cells displayed significant spatial information ($p < .01$; Figure 2A-B, Supplemental figure 5), as compared to 31.33% (323/1031, N = 6) in CA1 and 42,15% (86/ 204, N = 5) CA3 cells. Despite the LS's known involvement in feeding-related behaviors (Calderwood et al., 2020; Carus-Cadavieco et al., 2017; Sweeney and Yang, 2016; Xu et al., 2019) , we did not observe any increased number of place cells with fields around food zones, nor did we observe overrepresentation of objects or walls (Supplemental figure 6).

With theta-rhythmic cells in the LS having higher firing rates than theta-rhythm independent cells (Pedemonte et al., 1998), and the suggestion that theta-rhythmic cells could receive direct hippocampal inputs (though see Twery et al., 1990, 1992), we asked whether LS cells with higher firing rates were also more likely to be spatially modulated. Indeed, spatially-modulated cells were significantly more active than non-modulated cells (Mann-Whitney test, U = 342219, $p < .0001$; Supplemental figure 5G-H) and displayed a higher bursting index, defined as the probability of a cell being active, given it was already in an active state, or p(a|a), than non spatially modulated cells (Mann-Whitney test, U = 36876, $p < .0001$; Supplemental figure 5H).

We compared the place field properties of cells recorded in LS to those of the place cells we recorded in CA1 and CA3 (Figure 2). For each animal, we computed the portion of significantly positionally modulated cells per region, which was not significantly different across LS, dCA1, and dCA3 (one-way ANOVA, $F(2,34) = 0.499$, $p = .6110$, Figure 2B). As expected on the basis or prior results (Leutgeb and Mizumori, 2002; Takamura et al., 2006; Tingley and Buzsáki, 2018; Zhou et al., 1999), the within-session stability of LS cells was significantly lower than that of place cells recorded in CA1 and CA3 (Kruskal-Wallis, $H(3) = 49.44$, $p < .0001$; Figure 2C). Conversely, the activity of LS neurons was significantly higher than those of dCA1 and dCA3 principal cells (Kruskall-Wallis, $H(3) = 56.76$, $p < .0001$;

Figure 2D), and place fields were more dispersed (Kruskall-Wallis, H(3) = 93.21, $p < .0001$, Figure 2E).

When decoding the location of the animals using a bootstrapped sample of 100 cells from each region (Figure 2G), the decoder trained on data from LS performs significantly better than a decoder trained on shuffled data (two-way RM ANOVA, F(1,9) = 76.15, $p < .0001$ for main effect of shuffle), even when decreasing the number of neurons used to only 40 neurons, for both decoding error (two-way repeated-measures (RM) ANOVA, F(3,19) = 571.4, $p = 0.0024$ for main effect of shuffle, F(3,19) = 6.948, $p = 0.0024$ for main effect of number of included cells; Supplemental figure 4B left) and decoding agreement (two-way RM ANOVA, F(3,19) = 1059, $p < .0001$ for main effect of shuffle, F(3,19) = 10.06, $p = 0.0003$ for main effect of number of included cells; Supplemental figure 4B right). The same held true for decoders trained using CA1 or CA3 data respectively (two-way RM ANOVA, CA1: F(1,15) = 444.1, $p < .0001$ for main effect of shuffle, F(3,15) = 0.0706, $p = 0.97$ for number of included cells; CA3: F(1,5) = 239.1, $p < .0001$ for main effect of shuffle, F(3,5) = 1.129, $p = 0.42$ for main effect of region, Supplemental figure 4B). Strikingly, a decoder trained on data from LS does not perform significantly worse than a decoder trained on CA1 or CA3 data (F(2,9) = 0.3579, $p = 0.71$ for main effect of region; Figure 2H).

A subset of LS cells has stable spatial representations up to 8 days, similar to CA1

To test whether the LS and the hippocampus exhibit comparable evolutions of their spatial code over time, we recorded from CA1 and LS neurons in a novel open field over both short (3 days) and longer timescales (8 days, Figure 3A). We assessed the stability of the spatial map across sessions, and we observed a subset of LS place cells that were stable over time (Figure 3B). Correlating the tuning maps of aligned LS cell pairs over days lead to a significant increase in correlation value over days (two-way ANOVA, F(2, 1470) = 8.129, *p*

= 0.0003, main effect of time) with LS cells being statistically more stable than shuffled comparisons ($F(2,1470) = 197.3$, $p < .0001$, main effect of shuffle, Figure 3C). There was no significant increase in the proportion of place cells per animal over days (one-way ANOVA, $F(3,16) = 1.618$, $p = .2247$, Figure 3D). We observed the strongest within-session stability on day 3 (Kruskal-Wallis, $H(4) = 19.16$, $p = 0.0003$; Figure 3E), as well as a steady increase in spatial information (Kruskal-Wallis, $H(4) = 13.27$, $p = 0.0041$; Figure 3F). We computed the mean stability for each place cell pair recorded over multiple days (Figure 3G), and when comparing the mean tuning map correlation between day 1 and 8 for LS and CA1 place cells, we found no significant difference in their stability (unpaired t-test, $t(68) = 1.475$, $p = 0.1449$, Figure 3H). Together, this suggests that a subset of LS place cells codes for space over longer periods of time, similarly to what has been described for CA1 (Gonzalez et al., 2019; Ziv et al., 2013).

LS integrates direction, velocity, and acceleration information

In CA1, place cells have been found to carry directional (Acharya et al., 2016; Leutgeb et al., 2000; Muller et al., 1994) and speed-related information (Czurko et al., 1999; McNaughton et al., 1983; Iwase et al., 2020; Góis and Tort, 2018). Previous studies found that subsets of LS neurons show some degree of modulation by direction of travel (Zhou et al., 1999) as well as velocity and acceleration (Wirtshafter and Wilson, 2019) through correlative measures in spatial alternation or T-maze navigation tasks, where the relationship between cell activity patterns and movement-associated variables may be confounded with task-dependent variables. Here, we again employed an information-theoretic approach to compute the MI between calcium activity and each of these self-motion correlates in a subset of mice recorded during a 15-minute free foraging task in the open field. We found that 28.13% of LS cells are significantly modulated by direction (346/1230, N =19 mice, Figure 4A,

Supplemental figure 7), 18.70% by velocity (230/1230, Figure 4C) and 24.63% by acceleration (303/1230, Figure 4E). We compared the proportion of LS cells significantly modulated by each of these variables with the hippocampus, and observed no significant differences in the proportion of velocity (Kruskall-Wallis, $H(3) = 0.255$, $p = 0.88$) or acceleration (Kruskall-Wallis, $H(3) = 2.262$, $p = 0.32$) modulated cells. The proportion of directionally modulated cells was significantly different across regions (Kruskall-Wallis, $H(3) = 9.898$, $p = .0071$). We found a proportion of cells that were significantly tuned to more than one of these variables in both LS and hippocampus (Figure 4G, Supplemental figure 8), with 22.03 % of LS cells (271/1230) encoding more than one modality (Figure 4H). Together, this conjunctive coding for location, directionality, and velocity parameters indicates that LS cells fire in response to more complex navigational features, similarly to the hippocampus.

To understand the function of this downstream copy of the hippocampal spatial code, we assessed the downstream targets of hippocampal to LS projection. To this end, we transfected an anterograde, transsynaptic Cre-expressing AAV1 viral vector (Zingg et al., 2017) and assessed the second-order targets of the dorsal CA1-lateral septum (dCA1-LS) and dorsal CA3-LS (dCA3-LS) projections (Figure 5). For either dCA1 or dCA3 injections, we observed a direct disynaptic pathway from principal cells of the hippocampus to the medial septum (Figure 5A-B) and the hypothalamic regions (Figure 5C). We observed that dCA1-LS preferentially targets the LH, and dCA3-LS targets the hypothalamus more broadly as well as the nuclei of the medial zone. In order to determine whether the projections observed at the level of the LS with both our anterograde tracing approaches constituted passing fibers or synaptic connections, we used an AAV-Flex-Synaptag (Beier et al., 2015), a Cre-dependent viral construct to express mRuby in the cytosol and eGFP bound to synaptophysin, a protein primarily expressed in the presynaptic endings of cells participating in synaptic transmission

(Figure 5D). We transfected cells at the level of the dorsal LS and observed significant synaptophysin-bound projections in the medial septum (Figure 5E), confirming the existence of direct, functional projections to medial septum neurons. Together, our work shows that LS receives direct inputs from dorsal hippocampus and in turn projects to regions that are not directly receiving inputs from the hippocampus itself (Figure 5F).

LS-cells coding for spatial and idiothetic information are non-uniformly distributed

To map out the monosynaptic connections between hippocampal and LS neurons, we transfected an anterograde transsynaptic Cre-expressing AAV1 viral vector (Zingg et al., 2017), in either the dCA1 or dCA3 (Supplemental figure 10A). We subsequently injected a Cre-dependent eYFP expressing virus in the LS to visualize cells that receive direct hippocampal input (Supplemental figure 10B). Importantly, this approach allowed us to quantify the cells along the LS anterior-posterior and dorsal-ventral axis receiving direct hippocampal inputs, and assess the density of their distribution within the anterior regions of the LS (Bregma +1.0 to 0.0 anterior-posterior). Both dorsal dCA1 and dCA3 injections resulted in the strongest transfection of LS cell bodies in dorsal regions compared to intermediate and ventral LS (Supplemental figure 10D-F). Hence, the density of hippocampal innervation to the LS is a gradient along the dorsal-ventral and anterior-posterior axis, with dorsal-posterior LS neurons receiving more substantial dorsal hippocampal inputs.

Next, we sought whether LS place cells had spatial properties that were dependent on the localization of their recording. To measure this, we classified the location of GRIN lens implants along the dorsal-ventral and anterior-posterior axis (Figure 6A). Post-mortem histological verification of GRIN lens implant combined with within-animal analysis of the location of recorded cells enabled us to approximate the location of each recorded cell

(Figure 6B). While we observed no differences in cell activity characteristics, such as bursting index or activity probability along the anterior-posterior axis, medial-lateral or dorsal-ventral axis (Supplemental figure 11), we found a pronounced increase in the portion of stable place cells (within-session stability > .5) along the anterior-posterior axis (linear regression, $R^2 = 0.1272$, $p = 0.013$, the proportion of stable cells per 0.2 mm bin per animal, n = 24 mice, Figure 6C). On the other hand, we observed a similar gradient along the dorsal-ventral axis, with a larger proportion of stable place cells found at the more dorsal regions of the LS, although this trend failed to reach significance (linear regression, $R^2 = 0.129$, $p = .0848$, n = 24 mice, Figure 6C). Taken together, these data strongly suggest that regions of the LS that receive stronger innervation from the dorsal hippocampus have a larger proportion of cells that reliably encode space; thus it is likely that this information is directly inherited from the hippocampus.

We also assessed the topographical distribution of self-motion tuned cells within the LS. We observed a pronounced dorsal-ventral gradient in the distribution of stable (within-session stability > .5) directionally modulated cells (linear regression, $R^2 = 0.3837$ $p = 0.0061$, n = 17 mice, Figure 6C), with most directionally modulated cells located at the more dorsal regions of the LS, but we did not observe such a gradient along the anterior-posterior axis (linear regression, $R^2 = 0.014$, $p = .3542$, n = 24 mice, Figure 6C). Velocity modulated cells were mostly found at the ventral pole of the LS (linear regression, $R^2 = 0.1836$, $p = 0.0367$, n = 24), but no such gradient was found along the anterior-posterior axis (linear regression, $R^2 = .0075$, $p = .4481$, $n = 24$). Acceleration-modulated cells were found evenly distributed throughout the LS (DV: $R^2 = .0146$, $p = .2928$; AP: $R^2 = .00055$, $p = .7981$, n = 24 mice).

Discussion

While spatial coding has been extensively characterized in the hippocampal formation, how downstream regions integrate this information has only recently begun to receive attention. The LS has re-emerged as a critical region implicated in a space encoding network, although electrophysiological recordings of the LS in rats have led to disparate estimates of the quantity and quality of place cells in the region (Leutgeb and Mizumori, 2002; Wirtshafter and Wilson, 2019, 2020; Tingley and Buzsáki, 2018): LS place cells recorded on a circular track were described to be almost absent (Tingley and Buzsáki, 2018), but were found to be abundant in reward-seeking tasks (Wirtshafter and Wilson, 2019, 2020). Using calcium imaging and unbiased information metric and decoding approaches, we found that 38.01% of GABAergic LS cells robustly code for space during free exploration in an open field and 45.29% of cells during linear track alternation. In addition to spatial information, we found that the LS also reliably encodes velocity, acceleration, and directional information, suggesting that the LS encodes more complex navigational features than previously thought.

Neuronal representations in the hippocampus have been found to change over time, with place code ensembles changing rapidly: an estimated ~40% (Gonzalez et al., 2019) to ~75-85% (Ziv et al., 2013) of CA1 neurons were found to remap over days. In the posterior LS, we found a subpopulation of cells that display stable place fields over eight days, comparable to CA1 cells recorded under the same conditions. The functional role of such stability remains to be elucidated. One possibility is that this ensemble may mediate the stable encoding of contexts over longer durations of time, which could account for the critical importance of the LS for a number of spatial behaviors, including contextual fear conditioning (Besnard et al., 2019; Butler et al., 2015; Garcia et al., 1997; Reis et al., 2010; Vetere et al., 2017), context-reward associations (Luo et al., 2011b; McGlinchey and Aston-Jones, 2018) and radial-maze navigation tasks (Leutgeb and Mizumori, 1999; M'Harzi and

Jarrard, 1992). Previous work has hinted at a dorsal to ventral organization of the LS place code: electrophysiology studies recorded a slightly larger proportion of LS place cells in the more dorsal regions (Takamura et al., 2006). A complementary anatomical microstructure has been previously described for the rate-independent phase code in the LS, where the strength of the phase code increased as a function of recording depth along the dorsal-ventral axis (Buzsáki and Tingley, 2018). Here we find that lateral septal place cells are arranged along an anterior-posterior gradient similar to the gradient of hippocampal inputs into the LS – a finding that helps to reconcile the variation in previously reported estimates of LS place cell prevalence, which ranged between 5.3% of cells recorded along the dorsal-ventral axis (Tingley and Buzsáki, 2018) up to 56% recorded at the most dorsal level of the LS (Wirtshafter and Wilson, 2019). This pattern suggests that the inhibitory neurons of the LS may inherit a place code from the hippocampus, with subregions receiving dorsal hippocampal inputs being most similar to the classical hippocampal place cells. Despite this interconnectedness with the LH and previous reports of LS place cells being skewed towards reward in a spatial navigation task (Wirtshafter and Wilson, 2020), we did not observe any increased LS place cell overrepresentation around food zones during free exploration.

In addition to place cells, we observed significant proportions of velocity and acceleration modulated cells in the lateral septum. These cells have been previously described by others using correlative measures, although estimated proportions vary widely: for velocity tuning in reward-seeking tasks, estimates range from almost absent (Buzsáki and Tingley, 2018) to almost 60% of cells (Wirtshafter and Wilson, 2019). For acceleration, approximately 45% of LS cells were found to show some degree of correlation, with almost 30% of recorded cells correlated with both speed and acceleration (Wirtshafter and Wilson, 2019). Here, using information metrics and a free exploration task in which firing characteristics are not confounded with task parameters, we find that 18.70% of cells were

modulated by velocity and 24.63% by acceleration. Cells reliably coding for both velocity and acceleration were found to be relatively sparse (2%). Velocity and acceleration cells were distributed dissimilarly in the LS, with velocity cells being more abundant towards the ventral pole, whereas acceleration modulated cells were found to be distributed equally. This raises the question whether velocity and acceleration information are inherited from different areas upstream of the LS. Interestingly, cells coding for direction were more abundant towards the dorsal portion of the LS, but distributed equally along the anterior-posterior axis. Previous studies have identified classical head direction cells in multiple, well-described circuits, including the postsubiculum (Taube et al., 1990), anterodorsal thalamic nucleus (Taube, 1995), mammillary bodies (Stackman and Taube, 1998), and entorhinal cortex (Sargolini et al., 2006). A probable source of directional information to the LS is the entorhinal cortex (Allen Brain Connectivity Atlas, Oh et al., 2014). Our work supports the perspective that LS neurons combine a wide range of modalities and may form a complex representation of context over longer timescales than previously reported. In addition to space, velocity, and reward information, hippocampal pyramidal cells have been shown to encode variables such as time (Eichenbaum, 2014; Pastalkova et al., 2008), odor (Deshmukh and Bhalla, 2003; MacDonald et al., 2013) and sound frequency (Aronov et al., 2017). Whether this information is also relayed to the LS remains to be elucidated.

The question arises of what the function of could be having a region downstream of the hippocampus that expresses such seemingly similar coding characteristics. Previous work estimated the convergence of hippocampal efferents onto LS neurons to be 20 to 800 times more dense than to any of its cortical targets (Tingley and Buzsáki, 2018). Understanding how individual LS neurons integrate the thousands of synaptic inputs they receive from these hippocampal pyramidal neurons will be critical to understanding how the hippocampal map is processed downstream. Through the process of synaptic integration, a receiving neuron can

fire an action potential upon receiving sufficient synchronized excitatory input on its dendrites, leading to rapid depolarization of the cell. The activation of a LS neuron could thus require multiple hippocampal pyramidal cells to spike simultaneously or in close temporal proximity. Hippocampal pyramidal cells will fire concomitantly when their place fields are in overlapping regions or in close vicinity of another. Due to the high interconnectivity of LS GABAergic neurons (Alonso and Frotscher, 1989; Staiger and Nürnberger, 1989), the activation of one LS cell could subsequently lead to the inhibition of other neurons in the nucleus (Leroy et al., 2018; Phelan et al., 1989), thereby reducing noise. Thus, through this process of coincidence detection and recurrent inhibition, the spatial map could be compressed to be represented by a much lower number of cells. As such, the LS could accurately convey hippocampal information to downstream regions using a much sparser signal, thereby allowing for increased metabolic efficiency (Olshausen and Field, 2004) and more effective associative learning (Isely et al., 2010; Palm and Sommer, 2006; Zetsche).

Indeed, our tracing work shows LS cells receiving hippocampal inputs from principal cells in turn project directly to the LH and the MS. Although the existence of an LS-MS projection has long been debated (Leranth et al., 1992; Staiger and Nürnberger, 1991; Swanson and Cowan, 1977, 1979; Witter et al., 1992), we observed labeling at the level of the MS after transfection of dCA1-input and dCA3-input receiving LS cells providing strong support that principle cells of the hippocampus send indirect projections to the MS through LS neurons. This circuit is complementary to the well-described projections of hippocampal GABAergic interneurons directly to the MS which may play a key role in theta rhythm generation (Toth et al., 1993; Manseau et al., 2008). The MS plays a role in generating and propagating theta rhythms throughout the hippocampal formation (Leão et al., 2015; Patel et al., 2013; Robinson et al., 2016), which in turn organizes hippocampal place cell activity (Buzsáki, 2002), as well as a behavioral role in the initiation and velocity of locomotion

(Fuhrmann et al., 2015; Justus et al., 2017). It may be that the information on locomotion-related information reported in specific MS neurons (Justus et al., 2017) may originate from the LS. Moreover, we observed a direct projection from the LS to the hypothalamus, a highly connected region traditionally known as necessary for the regulation of feeding (Stuber and Wise, 2016), arousal and motivation (Burdakov and Peleg-Raibstein, 2020), and, more recently learning and memory (Aitta-Aho et al., 2016; Izawa et al., 2019; Kosse and Burdakov, 2019; Petrovich, 2018). The LH is crucial for the control of locomotion (Gladfelter and Brobeck, 1962; Grillner et al., 2008; Kosse et al., 2017; Sinnamon, 1993) and thought to mediate motivational and goal-directed processes underlying feeding (Carus-Cadavieco et al., 2017; Mahler et al., 2014; Mogenson et al., 1980; Stuber and Wise, 2016).

In summary, we have shown that the GABAergic cells of the LS may provide the hypothalamus and medial septum with information about location, direction, and speed, and therefore constitute a core node within a distributed spatial memory network. Within this network, the LS may be necessary for the translation of spatial information to goal-directed or environmentally appropriate actions necessary for survival.

Methods

Animals

All procedures were approved by the McGill University and Douglas Hospital Research Centre Animal Use and Care Committee and in accordance with the Canadian Council on Animal Care. Naive mice were housed individually on a 12-hour light/dark cycle at 22°C and 40% humidity with food and water ad libitum. All experiments were carried out during the light portion of the light/dark cycle. Both male and female mice were used for this study.

Virus injections

Mice, 8-16 weeks old, were anesthetized with isoflurane (5% induction, 0.5-2% maintenance) and placed in a stereotaxic frame (David Kopf Instruments). Body temperature was maintained with a heating pad, and eyes were hydrated with gel (Optixcare). Carprofen (10 ml/kg) was administered subcutaneously. All viral injections were performed using a glass pipette connected to a Nanoject III (Drummond) injector at a flow rate of 1 nL/second. All stereotaxic coordinates are taken from Bregma (in mm). After surgery, animals were continuously monitored until recovery. For three days after surgery, mice were provided with a soft diet supplemented with Carprofen for pain management (MediGel CPF, ~5mg/kg/day).

Virus-mediated expression of genetically encoded calcium indicator

Adeno-associated virus (AAV) of serotype 9 containing the genetically encoded calcium indicator (GECI) 6 fast (GCaMP6f) under a flex promoter was obtained from the University of Pennsylvania Vector Core (AAV2/9.Syn.Flex.GCaMP6f.WPRE.SV40, CS0641, Penn Vector Core via Addgene). Lateral septum viral injections were targeted at the following coordinates: Anterior LS, AP: 0.86; ML: 0.35; DV: -3.0; Intermediate LS, AP: 0.38; ML: 0.35; DV: -2.7, Posterior LS, AP: 0.10; ML: 0.35; DV: -2.5, with DV + or - .2 to adjust for more dorsal or ventral placement of injection. Lateral septum injections were done in VGAT-IRES-Cre transgenic mice (Slc32a1$^{tm2(cre)Lowl}$/J, JAX stock #016962). For hippocampal principal cell imaging, C57Bl/6J mice (JAX stock #000664) were injected with a viral vector specifically targeting GCaMP6f expression to CaMKII-positive cells (AAV5.CamKII.GCaMP6f.WPRE.SV40, Penn Vector Corde via Addgene, CS1024). GCaMP6f injections were targeted at the following coordinates: CA1, AP: -1.8; ML: 1.5; DV: -1.5; CA3, AP: -2.1; ML: 2.3; DV: -2.2.

Retrograde tracing

Retrograde tracing studies were done using a Cre-dependent retrograde Rabies tracing approach. Briefly, 100 nL of helper virus (AAVdj.hSyn.Flex.TVA.P2A.eGFP.2A.oG, NeuroPhotonics Center, Laval, Canada; Callaway, 2008; Wickersham et al., 2007) was injected in the LSd (coordinates as above) of VGAT-IRES-Cre transgenic mice (n = 5 animals, Slc32a1$^{tm2(cre)Lowl}$/J, JAX stock #016962). Cre specificity was tested by the NeuroPhotonics center. After 4 weeks of incubation time to allow for the complete expression of the helper virus, 200 nL of inactivated EnvA pseudotyped rabies virus coupled to mCherry was injected (RABV-EnvA-deltaG-mCherry, NeuroPhotonics Center) at the same coordinates as the helper virus injection, and brains were collected 7 days later.

Anterograde transsynaptic tracing

To distinguish synaptic targets from passing projection fibers of dCA1 and dCA3 within the LS, C57Bl/6J mice (JAX stock #000664) received a bilateral injection of transsynaptic Cre-inducing anterograde virus (AAV1-hSyn-Cre-WPRE-hGH, Penn Vector Core via Addgene, V24784) mixed with a Cre-dependent tdTom-expressing reporter virus to visualize injection sites (AAV2-Ef1a-flex-tdTomato, NeuroPhotonics Center, AAV602) in a 3:1 ratio, 80 nL total injection volume per hemisphere (n = 5 mice per group). Injections were targeted at the following coordinates: CA1: AP: -1.86; ML: 1.5; DV: -1.5; CA3: AP: -2.1; ML: 2.3; DV: -2.2. Following 1 week of incubation time, animals received a bilateral injection of a Cre-dependent anterograde vector in LS expressing enhanced yellow fluorescent protein (400 nL, bilateral, AP: 0.5; ML: 0.35; DV: -2.6, AAVdj-DIO-Cheta-eYFP, NeuroPhotonics Center, AAV938). Brains were collected and processed three weeks post-injection.

Synaptag tracing

To verify presence of synaptic connections at the level of the LS-MS projection, AAVdj-hSyn-flex-mRuby2-syp-eGFP construct (lot AAV799, NeuroPhotonics Center; Oh et al., 2014) was injected in the LS of CaMKIIα-Cre mice (B6.Cg-Tg(Camk2a-cre)T29-1Stl/J, JAX stock #005359), with 100 nL total injection volume injected at 1 nL/second. After 4 weeks of incubation time, animals were perfused, and brains were processed as described below.

GRIN lens implant and baseplate

Two to four weeks post GCaMP6f injection, a 0.5 mm diameter gradient refractive index (GRIN, Inscopix) lens was implanted above LS, dorsal CA1 or CA3, or a 1.8 mm GRIN (Edmund Optics) lens was implanted above dorsal CA1. For .5 mm lens implant, the lens was glued to an aluminium baseplate prior to the surgery, which provided two main advantages: 1) it allowed us to implant the baseplate/lens assembly in one surgery (instead of separate surgeries) and 2) during the surgery the miniscope (V3, miniscope.org) was used to image for fluorescence while lowering the lens. The mouse was anesthetized with isoflurane, and the skull was cleared. A ~.6 mm diameter hole was drilled in the skull at the level of the injection site. An anchor screw was placed above the contralateral cerebellum to stabilize the implant. The baseplate and GRIN combination were attached to the miniscope and together secured to the stereotaxic frame. After making a leading track using a .5 mm diameter needle, the implant was lowered in place. While lowering the GRIN lens into the tissue, and an increase in fluorescent signal indicates that the injection site has been reached. Both the GRIN lens and baseplate were permanently secured using C&B-Metabond (Patterson Dental). A plastic cap was used to protect the GRIN lens from scratching during the recovery period and in between recording sessions. The animal was given 4 - 6 weeks of recovery time before experiments started. LS implants were targeted at the following coordinates: Anterior LS, AP: 0.86; ML: 0.35; DV: -2.9; Intermediate LS, AP: 0.38; ML: 0.35; DV: -2.65; Posterior

LS, AP: 0.10; ML: 0.35; DV: -2.45; with DV + or - .2 to adjust for dorsal, ventral or intermediate targets; CA3 implants were targeted at AP: -2.1; ML: 2.2; DV: -2.2.

For 1.8 GRIN lens implantation, a ~2 mm diameter cranial window was prepared. Again, an anchor screw was used to secure the implant in place. After removing the dura, a portion of the cortex above the injection site was gently aspirated using a vacuum pump without applying pressure on the underlying hippocampal tissue. The 1.8 mm GRIN lens was lowered at the following coordinates: AP: -1.8; ML: 1.5; DV: -1.8. The GRIN lens was permanently attached to the skull using Metabond, and Kwik-Sil (World Precision Instruments) silicone adhesive was placed on the GRIN to protect it. On average 4 weeks post-implant, the silicone cap was removed and CA1 was imaged using a miniscope mounted with an aluminium base plate while the mouse was under light anesthesia (~0.5 % isoflurane) to allow the visualization of cell activity. When a satisfying field of view was found (large number of neurons, visible landmarks), the baseplate was cemented above the GRIN lens and a protective cap was used to protect the GRIN from scratches. Imaging would start approximately 1 week after baseplating.

Miniscope recordings

The animals were habituated by being gently handled for ~5 min per day for 3 days. Animals were then water or chow-scheduled (2h access per day). Miniscope recordings performed at 30 Hz for 15 minutes every day, with just one recording session per day to minimize photobleaching. For open field recordings, animals were freely foraging for randomly placed 10% sucrose or 10% sweetened condensed milk in water rewards.

Recording environments consisted of a 45 x 45 cm dark grey open field with visual cues, or a 49 x 49 cm white plexiglass open field, which was placed in different recording chambers. For linear track recordings, rewards (30 ul of 10% sucrose water) were placed at

each end of the 100 cm linear track, or a 130 cm linear track, and the mouse had to consume one reward before getting the next one delivered.

Miniscope and behavior video acquisition

Miniscopes (V3, miniscope.org) were assembled using open-source plans as described previously (miniscope.org, Cai et al., 2016; Ghosh et al., 2011). Imaging data were acquired using a CMOS imaging sensor (Aptina, MT9V032) and multiplexed through a lightweight coaxial cable. Data was acquired using a data acquisition (DAQ) box connected via a USB host controller (Cypress, CYUSB3013). Animal behavior was recorded using a webcam mounted above the environment. Calcium and behavioral data were recorded using Miniscope custom acquisition software (miniscope.org). The DAQ simultaneously acquired behavioral and cellular imaging streams at 30 Hz as uncompressed .avi files (1000 frames per file), and all recorded frames were timestamped in order to perform the subsequent alignment.

Histology

After completion of all experiments, animals were deeply anesthetized with ketamine/xylazine/acepromazide (100, 16, 3 mg/kg, respectively, intraperitoneal injection). Mice were then transcardially perfused with 4% paraformaldehyde in PBS (PFA). Brains were extracted and postfixed in PFA at 4 °C for a minimum of 48 hours. Brains were sectioned at 50 μm using a vibratome and cryoprotected in a solution of 30% ethylene glycol, 30% glycerol and 40% PBS until used.

Immunohistochemistry

Sections were washed 3 x 20 min in PGT (0.45% Gelatin and 0.25% Triton in 1x PBS) at room temperature. Next, primary antibodies (1:1000 goat anti-GFP from Novus Biologicals or 1:10 000 rabbit anti-RFP from VWR (Rockland) were incubated with PGT overnight at 4°C. Following 10, 20, and 40 min washes in PGT, sections were incubated with secondary antibodies (1:1000 donkey anti-goat coupled to A488 or 1:1000 donkey anti-rabbit coupled to A555, both from Molecular Probes) in PGT at room temperature for 1 hour. Sections were subsequently washed for 10 and 20 minutes in PGT and 30 minutes in PBS. Sections were then mounted on glass slides and permanently coverslipped with Fluoromount that contained DAPI.

Calcium imaging analysis

Calcium imaging videos were analyzed using the Miniscope Analysis pipeline (https://github.com/etterguillaume/MiniscopeAnalysis) as described previously (Etter et al., 2020; Pnevmatikakis and Giovannucci, 2017). Non-rigid motion correction was applied using NoRMCorre (Pnevmatikakis and Giovannucci, 2017), and videos were spatially downsampled (3x) before concatenation. Calcium traces were extracted using CNMFe (Zhou et al., 2017) using the following parameters: gSig = 3 pixels (width of gaussian kernel), gSiz = 20 pixels (approximate neuron diameter), background_model = 'ring', spatial_algorithm = 'hals', min_corr = 0.8 (minimum pixel correlation threshold), min_PNR = 8 (minimum peak-to-noise ratio threshold). After extraction, cells and traces were visually inspected, and cells with low signal to noise ratio were removed. Raw calcium traces were filtered to remove high-frequency fluctuations and binarized (normalized amplitude > 2 sd and the first-order derivative > 0, Etter et al., 2020).

Position data were inferred offline following the recording, using the red LED on the CMOS of the miniscope. A subset of behavioral videos were analyzed using DeepLabcut

through Python Integrated Miniscope Pipeline Notebook (PIMPN, available through https://github.com/etterguillaume/PIMPN) to extract head direction.

Activity and bursting index

Following the binarization of raw calcium traces, we compute the probability of a neuron to be active P(A) using the following formula:

$$P(A) = \frac{time\ active}{total\ time}$$

The bursting index was computed as the probability of a cell being active, given it was already in an active state, or P(A|A). The activity index is computed as the probability of a cell becoming active when it is in an inactive state, or P(A|I).

Spatial modulation

Space was binned (Position in open field: 17 x 17 bins of 3 cm; Position in linear track: 34 bins of 3 cm; velocity, min = 2.5 cm/s, max = 30 cm/s, 20 bins; acceleration: min = -2 cm/s^2, max = +2 cm/s^2 , 20 bins; head direction: 40 bins of 9°). Velocity was smoothed over thirty frames to reduce discontinuities. For head direction and positional information, all frames where velocity was < 5cm/s were excluded. The probability of being active P(A) informs on the activity rate of a neuron. Next, we compute the probability of spending time in a given bin *i* (spatial, velocity, acceleration or head direction bin).

$$P(S_i) = \frac{time\ in\ bin\ i}{total\ time}$$

Next, we compute the joint probability:

$$P(S_i \cap A) = \frac{time\ active\ while\ in\ bin\ i}{total\ time}$$

And the probability that a cell is active given the animal is in a bin:

$$P(A \mid S_i) = \frac{time\ active\ while\ in\ bin\ i}{time\ in\ state}$$

After plotting the binarized activity in space, we perform n = 1000 random circular permutations. Circular permutations are used to remove the temporal relationship between neuronal activity and behavior, but it preserves the temporal structure of calcium transients and therefore leads to more conservative results (as opposed to complete randomization of every data point, which inflates the significance value of results). In this case, the p-value corresponds to the number of datapoints from the shuffled distribution that are greater than the actual data for each bin, divided by the number of permutations (Cohen, 2014). A threshold of $p < .01$ is used to determine the significant data points that make up a significant place field. In our case, for a cell to be considered a place cell, at least one of the spatial bins must contain activity that is significantly non-random. To compute within-session stability, the halfway point in the recording was determined by taking the timestamps where half of the total number of binarized events for the session was reached. Tuning maps were computed for both the first and second half of the session using the methodology described above. A Gaussian smoothing filter ($\sigma = 3$) was used to smooth the tuning maps before computing a correlation between the two. A within-session correlation value of >.5 was considered a stable field.

Calculating mutual information content

Mutual information is used to describe the amount of information about one variable (spatial location, head direction, velocity or acceleration) through the observation of neuronal activity, and was calculated using the following formula:

$$MI = \sum_{i=1}^{M} \sum_{j=1}^{2} P(S_i \cap A_j) \times log2\left(\frac{P(S_i \cap A_j)}{P(S_i) \times P(A_j)}\right)$$

Where M is the total number of possible behavioral states, $P(S_i \cap A_j)$ is the joint probability of the animal being in bin i concurrently with activity level j. As we are using binarized activity, j can only be active or inactive. MI was calculated using 30 bootstrapped surrogates using 50 percent of the data (randomly chosen data points) with replacement, to allow for computation of mean MI and SEM. Next, the trace was circularly shuffled in order to calculate a shuffled MI and SEM. Cells were then sorted along with the magnitude of the difference between mean MI and mean shuffled MI, and a two-way ANOVA with a $p < .01$ threshold was used to determine whether the difference between the two numbers was significant in order for the cell to be deemed a significant place cell. In case the assumptions for parametric ANOVA are not met, the significance value was computed by taking the sum of the shuffled MI values of greater magnitude than actual MI values, divided by the number of shuffles.

Bayesian decoding

A Bayesian decoder was used to evaluate how well LS neural activity estimated the animal's location. We used decoding methods specifically adapted for calcium imaging data with binarized calcium transients (Etter et al., 2020). The training dataset was generated using 50% of the data, randomly chosen, using 30 bootstrap samples including 40, 60, 80 or 100 randomly chosen cells (Supplemental figure 4). The posterior probability density function, which is the probability that an animal is in a particular bin S_i , given the neural activity A is calculated using the following equation:

$$P(S_i \mid A) = \frac{P\ (A \mid S_i)\ \times\ P\ (S_i)}{P\ (A)}$$

P(S|A) is the posterior probability distribution of states given neuronal activity. No prior assumption is made about the location of the mouse on the linear track, P(S) is kept uniform to attribute equal probability for each location. Every neuron is assumed to be independent of

each other. To construct the tuning curves from multiple neurons, we use the following equation:

$$P\ (S \mid A)\ =\ \prod_{k\ =\ 1}^{N} \frac{P(A_k \mid S)\ \times\ P\ (S)}{P\ (A_k)}$$

With *P(S|A)* a vector of *a posteriori* behavioral states and *N* corresponding to the number of neurons used. For every neuron *k* the tuning curves are constructed, and corresponding posterior location probability can be derived.

To reconstruct the position of the mouse, we will consider the location associated with the maximum a posteriori:

$$\hat{y} =\ arg\ max\ exp\left[\sum_{k\ =1}^{N}\ log(\ 1 + \frac{P(A_k \mid S)\ \times\ P(S)}{P(A_k)}\ )\ -\ 1\right]$$

With the estimated state among all possible states S. We used a temporal filtering window in the open field of 1.5 seconds and in the linear track of 0.5 seconds to remove erratic jumps in the decoded position of the mouse. Decoding accuracy was measured as 1) decoding error and 2) decoding agreement. In one-dimensional space, decoding error was assessed as

$$decoding\ error\ =\ |\ decoded\ position\ -\ actual\ position\ |$$

In two-dimensional space, decoding error was assessed as

$$decoding\ error\ =\ (\sqrt{actual\ position\ -\ decoded\ position})^2$$

Decoding score was computed as

$$decoding\ score\ =\ \frac{mean\ (shuffled\ decoding\ error)\ -\ mean\ (decoding\ error)}{length\ of\ track}$$

Decoding agreement was defined as the portion of time where the exact location or head direction bin was successfully decoded:

$$decoding\ agreement\ =\ \frac{time\ points\ successfully\ decoded}{total\ time}$$

Tracking cells across sessions

Neurons were tracked over multiple days using a probabilistic method as previously described (Sheintuch et al., 2017). Briefly, spatial footprints were aligned using non-rigid alignment (transformation smoothness = 2) to correct for displacements of the brain or miniscope placement. After alignment, we considered candidate sets of cells to be the same neuron if their maximal distance was < 12 um, and the spatial correlation between sets of cells was > .65. Next, we visually identified candidate cell pairs across sessions and manually deleted those cell pairs that were erroneously selected (< 1% of cases). We assessed the stability of the spatial representation in LS using simple field correlation, which was assessed by correlating smoothed place fields of cell pairs. To generate the null hypothesis for place fields' displacements between pairs of days, we used the place fields tuning maps but shuffled cells identities over days (30 shuffles).

Materials availability

This study did not generate new unique reagents.

Data and Code availability

All data will be made publicly available. Code for cell extraction is available at https://github.com/etterguillaume/MiniscopeAnalysis. Code for behavior extraction is available at https://github.com/etterguillaume/PIMPN. Code for extraction of tuning curves and decoding were adapted from Etter et al. (2020) and can be downloaded at the following address: https://github.com/etterguillaume/CaImDecoding. All other code is available from the corresponding authors upon request.

Statistics

Statistics Statistical analyses were performed using Matlab (Mathworks) and GraphPad Prism version 6.00 (GraphPad Software, La Jolla, California USA). All data are presented as mean ± standard error of the mean (SEM) and statistical test details are described in the corresponding results. All t-tests are two-tailed. Normality distribution of each group was assessed using the Shapiro-Wilk normality test and parametric tests were used only when distributions were found normal, using Student's t-tests, one-way ANOVA or two-way ANOVA. For non-normal distributions, non-parametric tests Mann-Whitney or Kruskal-Wallis tests were performed and described where applicable. Significant main effects or interactions were followed up with appropriate post hoc testing using Bonferroni corrections were applicable. $p < 0.05$ was considered statistically significant, or $p < .01$ and described where applicable *, $p < 0.05$; **, $p < 0.01$; ***, $p < 0.001$, ****, $p < 0.0001$.

Funding

This work was supported by funding from the Canadian Institutes for Health Research (CIHR), Fonds de la Recherche en Santé du Québec (FRSQ), and the Natural Sciences and Engineering Research Council of Canada (NSERC). SVDV is supported by a Vanier Canada Graduate Scholarship and the Richard H. Tomlinson Doctoral Fellowship.

Acknowledgments

We thank Alexandra T. Keinath for valuable comments on a previous version of the manuscript. We thank Ke Cui for help with colony maintenance and mice perfusions, and members of the Williams lab for constructive feedback throughout the work. We also thank Daniel Aharoni (UCLA) for guidance in using the UCLA miniscope and Bruno Rivard for building the miniscopes. The present study used the services of the Molecular and Cellular Microscopy Platform at the DHRC.

Competing interests

The authors declare no competing interests.

References

Aitta-Aho, T., Pappa, E., Burdakov, D., and Apergis-Schoute, J. (2016). Cellular activation of hypothalamic hypocretin/orexin neurons facilitates short-term spatial memory in mice. Neurobiol. Learn. Mem. *136*, 183–188.

Alonso, J.R., and Frotscher, M. (1989). Organization of the septal region in the rat brain: a Golgi EM study of lateral septal neurons. J. Comp. Neurol. *286*, 472–487.

Anthony, T.E., Dee, N., Bernard, A., Lerchner, W., Heintz, N., and Anderson, D.J. (2014). Control of stress-induced persistent anxiety by an extra-amygdala septohypothalamic circuit. Cell *156*, 522–536.

Aronov, D., Nevers, R., and Tank, D.W. (2017). Mapping of a non-spatial dimension by the hippocampal-entorhinal circuit. Nature *543*, 719–722.

Beier, K.T., Steinberg, E.E., Deloach, K.E., Kremer, E.J., Malenka, R.C., Luo, L., Beier, K.T., Steinberg, E.E., Deloach, K.E., Xie, S., et al. (2015). Circuit Architecture of VTA Dopamine Neurons Revealed by Systematic Input-Output Mapping Article Circuit Architecture of VTA Dopamine Neurons Revealed by Systematic Input-Output Mapping. Cell *162*, 622–634.

Bender, F., Gorbati, M., Cadavieco, M.C., Denisova, N., Gao, X., Holman, C., Korotkova, T., and Ponomarenko, A. (2015). Theta oscillations regulate the speed of locomotion via a hippocampus to lateral septum pathway. Nat. Commun. *6*, 8521.

Besnard, A., Gao, Y., Kim, M.T., Twarkowski, H., Reed, A.K., Langberg, T., Feng, W., Xu, X., Saur, D., Zweifel, L.S., et al. (2019). Dorsolateral septum somatostatin

interneurons gate mobility to calibrate context-specific behavioral responses. Nat. Neurosci. *22*, 436–446.

Bredewold, R., Schiavo, J.K., van der Hart, M., Verreij, M., and Veenema, A.H. (2015). Dynamic changes in extracellular release of GABA and glutamate in the lateral septum during social play behavior in juvenile rats: Implications for sex-specific regulation of social play behavior. Neuroscience *307*, 117–127.

Brito, G.N.O., and Thomas, G.J. (1981). T-maze alternation, response patterning, and septo-hippocampal circuitry in rats. Behav. Brain Res. *3*, 319–340.

Burdakov, D., and Peleg-Raibstein, D. (2020). The hypothalamus as a primary coordinator of memory updating. Physiol. Behav. *223*, 112988.

Butler, C.W., Wilson, Y.M., Gunnersen, J.M., and Murphy, M. (2015). Tracking the fear memory engram: Discrete populations of neurons within amygdala, hypothalamus, and lateral septum are specifically activated by auditory fear conditioning. Learn. Mem. *22*, 370–384.

Buzsáki, G. (2002). Theta oscillations in the hippocampus. Neuron *33*, 325–340.

Buzsáki, G., and Tingley, D. (2018). Space and Time: The Hippocampus as a Sequence Generator. Trends Cogn. Sci.

Cai, D.J., Aharoni, D., Shuman, T., Shobe, J., Biane, J., Song, W., Wei, B., Veshkini, M., La-Vu, M., Lou, J., et al. (2016). A shared neural ensemble links distinct contextual memories encoded close in time. Nature *534*, 115–118.

Calderwood, M.T., Tseng, A., and Glenn Stanley, B. (2020). Lateral septum mu opioid receptors in stimulation of feeding. Brain Res. *1734*, 146648.

Callaway, E.M. (2008). Transneuronal circuit tracing with neurotropic viruses. Curr. Opin. Neurobiol. *18*, 617–623.

Carus-Cadavieco, M., Gorbati, M., Ye, L., Bender, F., van der Veldt, S., Kosse, C., Börgers,

C., Lee, S.Y., Ramakrishnan, C., Hu, Y., et al. (2017). Gamma oscillations organize top-down signalling to hypothalamus and enable food seeking. Nature *542*, 232–236.

Chee, S.-S.A., Menard, J.L., and Dringenberg, H.C. (2015). The lateral septum as a regulator of hippocampal theta oscillations and defensive behavior in rats. J. Neurophysiol. *113*, 1831–1841.

Clemens, A.M., Wang, H., and Brecht, M. (2020). The lateral septum mediates kinship behavior in the rat. Nat. Commun. *11*, 1–11.

Cohen, M.X. (2014). Analyzing Neural Time Series Data: Theory And Practice. (Cambridge, MA: The MIT Press).

Deshmukh, S.S., and Bhalla, U.S. (2003). Representation of odor habituation and timing in the hippocampus. J. Neurosci. *23*, 1903–1915.

Eichenbaum, H. (2014). Time cells in the hippocampus: A new dimension for mapping memories. Nat. Rev. Neurosci. *15*, 732–744.

Etter, G., Manseau, F., and Williams, S. (2020). A Probabilistic Framework for Decoding Behavior From in vivo Calcium Imaging Data. Front. Neural Circuits *14*, 1–16.

Fuhrmann, F., Justus, D., Sosulina, L., Kaneko, H., Beutel, T., Friedrichs, D., Schoch, S., Schwarz, M., Fuhrmann, M., and Remy, S. (2015). Locomotion, Theta Oscillations, and the Speed-Correlated Firing of Hippocampal Neurons Are Controlled by a Medial Septal Glutamatergic Circuit. Neuron *86*, 1253–1264.

Garcia, R., Vouimba, R.M., and Jaffard, R. (1997). Contextual conditioned fear blocks the induction but not the maintenance of lateral septal LTP in behaving mice. J. Neurophysiol. *78*, 76–81.

Ghosh, K.K., Burns, L.D., Cocker, E.D., Nimmerjahn, A., Ziv, Y., Gamal, A. El, and Schnitzer, M.J. (2011). Miniaturized integration of a fluorescence microscope. Nat. Methods *8*, 871–878.

Gladfelter, W.E., and Brobeck, J.R. (1962). Decreased spontaneous locomotor activity in the rat induced by hypothalamic lesions. Am. J. Physiol. *203*, 811–817.

Gonzalez, W.G., Zhang, H., Harutyunyan, A., and Lois, C. (2019). Persistence of neuronal representations through time and damage in the hippocampus. Science (80-.). *365*, 821–825.

Grillner, S., Wallén, P., Saitoh, K., Kozlov, A., and Robertson, B. (2008). Neural bases of goal-directed locomotion in vertebrates-An overview. Brain Res. Rev. *57*, 2–12.

Howard, M.W., and Kahana, M.J. (2002). A distributed representation of temporal context. J. Math. Psychol. *46*, 269–299.

Isely, G., Hillar, C.J., and Sommer, F.T. (2010). Deciphering subsampled data: Adaptive compressive sampling as a principle of brain communication. Adv. Neural Inf. Process. Syst. 23 24th Annu. Conf. Neural Inf. Process. Syst. 2010, NIPS 2010 1–9.

Izawa, S., Chowdhury, S., Miyazaki, T., Mukai, Y., Ono, D., Inoue, R., Ohmura, Y., Mizoguchi, H., Kimura, K., Yoshioka, M., et al. (2019). REM sleep-active MCH neurons are involved in forgetting hippocampusdependent memories. Science (80-.). *365*, 1308–1313.

Justus, D., Dalügge, D., Bothe, S., Fuhrmann, F., Hannes, C., Kaneko, H., Friedrichs, D., Sosulina, L., Schwarz, I., Elliott, D.A., et al. (2017). Glutamatergic synaptic integration of locomotion speed via septoentorhinal projections. Nat. Neurosci. *20*, 16–19.

Kita, T., Nishijo, H., Eifuku, S., Terasawa, K., and Ono, T. (1995). Place and contingency differential responses of monkey septal neurons during conditional place-object discrimination. J. Neurosci. *15*, 1683–1703.

Kosse, C., and Burdakov, D. (2019). Natural hypothalamic circuit dynamics underlying object memorization. Nat. Commun. *10*, 1–8.

Kosse, C., Schöne, C., Bracey, E., and Burdakov, D. (2017). Orexin-driven GAD65 network of the lateral hypothalamus sets physical activity in mice. Proc. Natl. Acad. Sci. U. S. A. *114*, 4525–4530.

Leão, R.N., Targino, Z.H., Colom, L. V., and Fisahn, A. (2015). Interconnection and synchronization of neuronal populations in the mouse medial septum/diagonal band of Broca. J. Neurophysiol. *113*, 971–980.

Leranth, C., Deller, T., and Buzsáki, G. (1992). Intraseptal connections redefined: lack of a lateral septum to medial septum path. Brain Res. *583*, 1–11.

Leroy, F., Park, J., Asok, A., Brann, D.H., Meira, T., Boyle, L.M., Eric, W., and Siegelbaum, S.A. (2018). A circuit from hippocampal CA2 to lateral septum disinhibits social aggression. Nature *564*, 213–218.

Leutgeb, S., and Mizumori, S. (1999). Excitotoxic septal lesions result in spatial memory deficits and altered flexibility of hippocampal single-unit representations. J. Neurosci. *19*, 6661–6672.

Leutgeb, S., and Mizumori, S. (2002). Context-specific spatial representations by lateral septal cells. Neuroscience *112*, 655–663.

Luo, A.H., Tahsili-Fahadan, P., Wise, R.A., Lupica, C.R., and Aston-Jones, G. (2011a). Linking context with reward: a functional circuit from hippocampal CA3 to ventral tegmental area. Science (80-.). *333*, 353–358.

Luo, A.H., Tahsili-fahadan, P., Wise, R.A., Lupica, C.R., and Aston-jones, G. (2011b). Supporting Online Material for CA3 to Ventral Tegmental Area.

M'Harzi, M., and Jarrard, L.E. (1992). Effects of medial and lateral septal lesions on acquisition of a place and cue radial maze task. Behav. Brain Res. *49*, 159–165.

MacDonald, C.J., Carrow, S., Place, R., and Eichenbaum, H. (2013). Distinct hippocampal time cell sequences represent odor memories in immobilized rats. J. Neurosci. *33*,

14607–14616.

Mahler, S. V., Moorman, D.E., Smith, R.J., James, M.H., and Aston-Jones, G. (2014). Motivational activation: A unifying hypothesis of orexin/hypocretin function. Nat. Neurosci. *17*, 1298–1303.

Mankin, E.A., Diehl, G.W., Sparks, F.T., Leutgeb, S., and Leutgeb, J.K. (2015). Hippocampal CA2 Activity Patterns Change over Time to a Larger Extent than between Spatial Contexts. Neuron *85*, 190–202.

McGlinchey, E.M., and Aston-Jones, G. (2018). Dorsal hippocampus drives context-induced cocaine seeking via inputs to Lateral Septum. Neuropsychopharmacology *43*, 987–1000.

Mogenson, G.J., Jones, D.L., and Yim, C.Y. (1980). From motivation to action: Functional interface between the limbic system and the motor system. Prog. Neurobiol. *14*, 69–97.

Nishijo, H., Kita, T., Tamura, R., Uwano, T., and Terasawa, K. (1997). Septal Neuronal Responses Related to Spatial Representation in Monkeys. Hippocampus *464*, 460–464.

Oh, S.W., Harris, J.A., Ng, L., Winslow, B., Cain, N., Mihalas, S., Wang, Q., Lau, C., Kuan, L., Henry, A.M., et al. (2014). A mesoscale connectome of the mouse brain. Nature *508*, 207–214.

Olshausen, B.A., and Field, D.J. (2004). Sparse coding of sensory inputs. Curr. Opin. Neurobiol. *14*, 481–487.

Palm, G., and Sommer, F.T. (2006). Associative Data Storage and Retrieval in Neural Networks. In Models of Neural Networks III. Physics of Neural Networks, Domany E., J.L. van Hemmen, and K. Schulten, eds. (Springer, New York, NY.), p.

Pastalkova, E., Itskov, V., Amarasingham, A., and Buzsáki, G. (2008). Internally generated

cell assembly sequences in the rat hippocampus. Science (80-.). *321*, 1322–1328.

Patel, J., Schomburg, E.W., Bere, A., and Fujisawa, S. (2013). Local Generation and Propagation of Ripples along the Septotemporal Axis of the Hippocampus. *33*, 17029–17041.

Petrovich, G.D. (2018). Lateral hypothalamus as a motivation-cognition interface in the control of feeding behavior. Front. Syst. Neurosci. *12*, 1–7.

Phelan, K.D., Hasuo, H., Twery, M.J., and Gallagher, J.P. (1989). Projection neurons in the rat dorsolateral septal nucleus possess recurrent axon collaterals. Neurosci. Lett. *97*, 259–265.

Pnevmatikakis, E.A., and Giovannucci, A. (2017). NoRMCorre: An online algorithm for piecewise rigid motion correction of calcium imaging data. J. Neurosci. Methods *291*, 83–94.

Rawlins, J.N.P., and Olton, D.S. (1982). The septo-hippocampal system and cognitive mapping. Behav. Brain Res. *5*, 331–358.

Reis, D.G., Scopinho, A.A., Guimarães, F.S., Corrêa, F., and Resstel, L.B.M. (2010). Involvement of the lateral septal area in the expression of fear conditioning to context. Learn. Mem. *17*, 134–138.

Risold, P.Y., and Swanson, L.W. (1996). Structural evidence for functional domains in the rat hippocampus. Science (80-.). *272*, 1484–1486.

Risold, P.Y., and Swanson, L.W. (1997). Connections of the rat lateral septal complex. Brain Res. Rev. *24*, 115–195.

Robinson, J., Manseau, F., Ducharme, G., Vigneault, E., El Mestikawy, S., and Williams, S. (2016). Optogenetic Activation of Septal Glutamatergic Neurons Drive Hippocampal Theta Rhythms. *36*, 3016–3023.

Rubin, A., Geva, N., Sheintuch, L., and Ziv, Y. (2015). Hippocampal ensemble dynamics

timestamp events in long-term memory. Elife *4*, 1–16.

Sargolini, F., Fyhn, M., Hafting, T., McNaughton, B.L., Witter, M.P., Moser, M.B., and Moser, E.I. (2006). Conjunctive representation of position, direction, and velocity in entorhinal cortex. Science (80-.). *312*, 758–762.

Sheintuch, L., Rubin, A., Brande-Eilat, N., Geva, N., Sadeh, N., Pinchasof, O., and Ziv, Y. (2017). Tracking the Same Neurons across Multiple Days in Ca2+Imaging Data. Cell Rep. *21*, 1102–1115.

Sinnamon, H.M. (1993). Preoptic and hypothalamic neurons and the initiation of locomotion in the anesthetized rat. Prog. Neurobiol. *41*, 323–344.

Sparks, P., and Ledoux, J. (2000). The septal complex as seen through the context of fea, In: the behavioral neuroscience of the septal region (Springer-Verlag).

Stackman, R.W., and Taube, J.S. (1998). Firing properties of rat lateral mammillary single units: Head direction, head pitch, and angular head velocity. J. Neurosci. *18*, 9020–9037.

Staiger, J.F., and Nürnberger, F. (1989). Pattern of afferents to the lateral septum in the guinea pig. Cell Tissue Res. *257*, 471–490.

Staiger, J.F., and Nürnberger, F. (1991). The efferent connections of the lateral septal nucleus in the guinea pig: intrinsic connectivity of the septum and projections to other telencephalic areas. Cell Tissue Res. *264*, 415–426.

Stanton, M.E., Thomas, G.J., and Brito, G.N.O. (1984). Posterodorsal septal lesions impair performance on both shift and stay working memory tasks. Behav. Neurosci. *98*, 405–415.

Stuber, G.D., and Wise, R.A. (2016). Lateral Hypothalamic Circuits for Feeding and Reward. Nat. Neurosci. *19*, 198–205.

Swanson, L.W., and Cowan, W.M. (1977). An Autoradiographic Study of the Organization

of the Efferent Connections of the Hippocampal Formation in the Rat. J. Comp. Neur. *172*, 49–84.

Swanson, L.W., and Cowan, W.M. (1979). The Connections of the Septal Region in the Rat. J. Comp. Neur. *186*, 621–656.

Sweeney, P., and Yang, Y. (2016). An Inhibitory Septum to Lateral Hypothalamus Circuit That Suppresses Feeding. J. Neurosci. *36*, 11185–11195.

Takamura, Y., Tamura, R., Zhou, T.L., Kobayashi, T., Tran, A.H., Eifuku, S., and Ono, T. (2006). Spatial Firing Properties of Lateral Septal Neurons. *644*, 635–644.

Taube, J.S. (1995). Head direction cells recorded in the anterior thalamic nuclei of freely moving rats. J. Neurosci. *15*, 70–86.

Taube, J., Muller, R., and Ranck, J. (1990). Head-direction cells recorded from the postsubiculum in freely moving rats. I. Description and quantitative analysis. J. Neurosci. *10*, 420–435.

Thomas, G.J. (1979). Comparison of effects of small lesions in posterodorsal septum on spontaneous and rerun correction (contingently reinforced) alternation in rats. J. Comp. Physiol. Psychol. *93*, 685–694.

Thomas, G.J., and Brito, G.N. (1980). Recovery of delayed alternation in rats after lesions in medial frontal cortex and septum. J. Comp. Physiol. Psychol. *94*, 808–818.

Tingley, D., and Buzsáki, G. (2018). Transformation of a Spatial Map across the Hippocampal-Lateral Septal Circuit. Neuron *98*, 1229-1242.e5.

Trent, N.L., and Menard, J.L. (2010). The ventral hippocampus and the lateral septum work in tandem to regulate rats' open-arm exploration in the elevated plus-maze. Physiol. Behav. *101*, 141–152.

Vetere, G., Kenney, J.W., Tran, L.M., Xia, F., Steadman, P.E., Parkinson, J., Josselyn, S.A., and Frankland, P.W. (2017). Chemogenetic Interrogation of a Brain-wide Fear

Memory Network in Mice. Neuron *94*, 363-374.e4.

Wickersham, I.R., Finke, S., Conzelmann, K.K., and Callaway, E.M. (2007). Retrograde neuronal tracing with a deletion-mutant rabies virus. Nat. Methods *4*, 47–49.

Wirtshafter, H.S., and Wilson, M.A. (2019). Locomotor and Hippocampal Processing Converge in the Lateral Septum. Curr. Biol. *29*, 3177-3192.e3.

Wirtshafter, H.S., and Wilson, M.A. (2020). Differences in reward biased spatial representations in the lateral septum and hippocampus. Elife *9*, 1–20.

Witter, M.P., Daelmans, H.E., Jorritsma-Byham, B., Staiger, J.F., and Wouterlood, F.G. (1992). Restricted origin and distribution of projections from the lateral to the medial septal complex in rat and guinea pig. Neurosci. Lett. *148*, 164–168.

Xu, Y., Lu, Y., Cassidy, R.M., Mangieri, L.R., Zhu, C., Huang, X., Jiang, Z., Justice, N.J., Xu, Y., Arenkiel, B.R., et al. (2019). Identification of a neurocircuit underlying regulation of feeding by stress-related emotional responses. Nat. Commun. *10*.

Zetsche, C. Sparse coding: the link between low level vision and associative memory. In Parallel Processing in Neural Systems and Computers, R. Eckmiller, G. Hartmann, and G. Hauske, eds. (Elsevier, Amsterdam, Holland), p.

Zhao, C., Eisinger, B., and Gammie, S. (2013). Characterization of GABAergic Neurons in the Mouse Lateral Septum: A Double Fluorescence In Situ Hybridization and Immunohistochemical Study Using Tyramide Signal Amplification. PLoS One *8*, 1–24.

Zhou, P., Resendez, S.L., Rodriguez-Romaguera, J., Jimenez, J.C., Neufeld, S.Q., Stuber, G.D., Hen, R., Kheirbek, M.A., Sabatini, B.L., Kass, R.E., et al. (2017). Efficient and accurate extraction of in vivo calcium signals from microendoscopic video data.

Zhou, T.L., Tamura, R., Kuriwaki, J., and Ono, T. (1999). Comparison of Medial and Lateral Septal Neuron Activity During Performance of Spatial Tasks in Rats. *234*, 220–234.

Zingg, B., Chou, X. lin, Zhang, Z. gang, Mesik, L., Liang, F., Tao, H.W., and Zhang, L.I. (2017). AAV-Mediated Anterograde Transsynaptic Tagging: Mapping Corticocollicular Input-Defined Neural Pathways for Defense Behaviors. Neuron *93*, 33–47.

Ziv, Y., Burns, L.D., Cocker, E.D., Hamel, E.O., Ghosh, K.K., Kitch, L.J., Gamal, A. El, and Schnitzer, M.J. (2013). Long-term dynamics of CA1 hippocampal place codes. Nat. Neurosci. *16*, 264–266.

Main figures

Figure 1: LS shares spatial coding characteristics with its main hippocampal inputs CA1 and CA3 during goal directed navigation in a 1D environment. A) Retrograde rabies tracing injection site, blue = DAPI staining, green = TVA.oG coupled to an enhanced green fluorescent protein (eGFP), red = Rabies coupled to mCherry, orange: starter cells expressing both TVA.oG.eGFP and Rabies.mCherry. B) Retrograde transfection in the dorsal hippocampus, coronal section. Bottom left: example of transfected CA1 pyramidal cell, bottom right: transfected CA3 pyramidal cells. (For additional images see Supplemental figure 1.) C) Top: Diagram of one-photon calcium recording setup in LS, CA1 and CA3 in freely behaving mice, middle: histological verification of implantation site and bottom: extracted calcium transients for LS, CA1 and CA3. D) Top: Recoding strategy in these animals, with animal alternating left and right trajectories to obtain a sucrose reward on a 100 or 130 cm linear track. Bottom: Probability of an example cell to be active given the location on the linear track (red) with 95% upper and lower percentile (grey). Examples shown are

from two different LS mice, and a representative place cell from one CA1 and CA3 animal each. F) Proportion of significantly spatially modulated cells for each animal for each recording region. Total recorded cells: LS: n = 1030 cells, N = 15 mice. CA1: n = 1148 cells, N = 5 mice, CA3: n = 144 cells, N = 2 mice. G) Split half stability of recorded spatial cells in each region and right: probability being active (LS: n = 475 cells, CA1: n = 336 cells, CA3: n = 47 cells). H) Top: Posterior probabilities for each frame estimated from binarized calcium activity, bottom: corresponding actual (green) and decoded (red) location. I) Schematic representation of bootstrapping approach. J) Method for computing the Euclidean distance mean decoding error in cm for each bootstrapped estimate and mean decoding agreement for each bootstrapped estimate for open field recordings. K) Decoding error for actual vs shuffled dataset (30 times bootstrapped sample of 60 cells, LS: N = 7 mice, CA1: N =5 mice, CA3: LS = 2 mice). L) Mean decoding score each region, *, $p < .05$, **, $p < .01$, ****, $p < .0001$, Test used in F-G, Kruskal-Wallis, K, paired t-test, L, one-way ANOVA.

Figure 2: LS shares spatial coding characteristics with its main hippocampal inputs CA1 and CA3 during free exploration in a 2D environment. A) Tuning curves of example place cells recorded from LS, dorsal CA1 and dorsal CA3 in a 45 cm open field (3 cm bins). B) Proportion of place cells per animal (LS: n = 1899 cells from N = 28 mice; dCA1: n = 1229 cells, N = 6 mice; dCA3: n = 204 cells, N = 4 mice). C) Within session stability for spatial cells (LS: n = 734 place cells from N = 28 mice; dCA1: n = 424 place cells, N = 6 mice; dCA3: n = 86 place cells, N = 4 mice). D) Probability of being active for spatial cells (LS: n = 734 place cells from N = 28 mice; dCA1: n = 424 place cells, N = 6 mice; dCA3: n = 86 place cells, N = 4 mice). E) Left: mean dispersion computation, right: mean dispersion for spatial cells (LS: n = 734 place cells from N = 28 mice; dCA1: n = 424 place cells, N = 6 mice; dCA3: n = 86 place cells, N = 4 mice). F) Bootstrapping approach using 100 cells. G)

Method for computing the mean decoding error and mean decoding agreement for each bootstrapped estimate using 100 cells. H) Mean decoding error for LS (N = 6), CA1 (N =4) and CA3 (N = 2). **, $p < .01$, ***, $p < .001$, ****, $p < .0001$, Test used in B, one-way ANOVA, C-E, Kruskal-Wallis, Dunn's multiple comparison test. H, two-way ANOVA, Sidak's multiple comparisons test.

Figure 3: LS place code remains similar to CA1 over longer periods of time. A) Experimental setup (top) and aligned spatial footprints of cells recorded over days (bottom). B) Tuning maps for two sets of stable cells recorded over all days, with each row being one aligned cell. Tuning map correlation indicated at the bottom. C) Tuning map correlation for all aligned cells (black) versus shuffled cells (red) for progressive days (day 1, n = 562; day 2, n = 600; day 3, n = 477; day 8, n = 492, n = 5 mice). D) Proportion of place cells recorded for each day. Each dot is an animal (N = 5). E) Within session stability for each place cell for all recorded cells (day 1, n = 181; day 2, n = 172; day 3, n = 178; day 8, n = 209, N = 5 mice). F) Average MI for each day for all recorded cells (day 1, n = 562; day 2, n = 600; day 3, n = 477; day 8, n = 492, n = 5 mice). G) Matrix of mean tuning map correlation for all aligned place cells recorded in LS (N = 3 mice) and CA1 (N = 1 mouse). H) Tuning map correlation between day 1 and day 8 for all aligned place cells recorded in LS vs CA1 (LS: 42 cells, n = 3 mice, CA1: 28 cells, n = 1 mouse). *, $p < .05$, **, $p < .01$, ****, $p < .0001$. Test used in C, two-way ANOVA, Sidak's multiple comparisons test, D, one-way ANOVA, E-F, Kruskall Wallis test, with Dunn's multiple comparison test, H, unpaired t-test.

Figure 4: LS GABAergic cells encode direction, speed, and acceleration. A) Left: Activity of an example LS neuron during free exploration in an open field, top: head direction (HD, red), middle: binarized activity (yellow), bottom: raw calcium activity (blue). Right:

Corresponding polar plot indicating the probability of the cell being active as a function of the animals' HD with (black, p(active | bin), red lines indicate 95% upper and lower percentile. MI calculated using 9° bins. Supplemental figure 7. B) Proportion of significantly directionally modulated cells in LS, dCA1 and dCA3. C) Left: Activity of an example LS neuron during free exploration modulated by velocity (top, red), middle: binarized activity (yellow), bottom: raw calcium activity (blue). Right: Tuning curve for velocity for the example cell (red) with 95% upper and lower percentile in grey. MI calculated using 20 bins. D) Proportion of significantly speed modulated cells in LS, dCA1 and dCA3. E) Left: Activity of an example LS neuron during free exploration modulated by acceleration (top, red), middle: binarized activity (yellow), bottom: raw calcium activity (blue). Right: Tuning curve for acceleration for the example cell (red) with 95% upper and lower percentile in grey. MI calculated using 20 bins. F) Comparison of proportions of significantly modulated cells for region. G) Example of an LS cell that is both significantly head direction modulated (left), as well as spatially modulated (right). H) Left: Proportion of cells that are significantly modulated by only one modality (grey), two modalities (yellow), three (red) or all 4 of the investigated variables (black). The number above the bars indicates the absolute number of cells found to be modulated in the total population (n = 1230 cells, N = 19 mice). Right: absolute proportion of cells modulated by any combination of variables. Test used in B, D, F: Kruskal-Wallis test with Dunn's multiple comparisons test. *, $p < .05$. D = direction, A = acceleration, S = spatial coding, V = velocity.

Figure 5: LS cells receiving hippocampal inputs project directly to hypothalamus and medial septum. A) Diagram of dual-viral injection strategy for anterograde transsynaptic tracing. The diagram is based on dorsal CA1 targeted injection, dCA3 is also used for injections, together with coronal sections showing primary injection site in dorsal CA1 (top)

or dorsal CA3 (bottom). Red = tdTom expression, blue = DAPI, with zoomed images showing transfected cell bodies are predominantly located in the pyramidal layer (bottom). B) eYFP-positive cell bodies at the anterior dorsal LS and fibers at the level of the medial septum following dCA1 injection (left) and dCA3 injection (right). Inset left: eYFP-positive fibers at the level of MS. C) Second-order transfection is seen bilaterally at the level of the lateral hypothalamus following dCA1 injection (left) and dCA3 injection (right). D) Injection strategy for Cre-dependent AAV. Synaptag mediated tracing in the LS. E) Coronal section of transfection at the level of dorsal LS, with synaptophysin-bound eYFP at the MS. Top right: Zoomed images showing transfection at the injection site. Bottom right: eYFP-positive fibers. F) Schematic with proposed connections of the LS within the hippocampal network. Scale bars: B, left and right: 800 μm. C, left and right: 500 μm/ DM = dorsomedial hypothalamic nucleus, 3V = third ventricle, LH = lateral hypothalamus.

Figure 6: LS-cells coding for spatial and idiothetic information are non-uniformly distributed along the dorsal-ventral and anterior-posterior axis. A) Strategy to record from different anterior-posterior levels in LS (left) and implantation sites covered. B) Strategy to approximate cell location. Background: Maximal projection of representative recording, red: outline of approximated GRIN lens position, white: distance from the center of the GRIN lens to the cells of interest. C) Top: For .2 mm bins along dorsal-ventral axis, proportion of stable (within-session stability > .5) place cells (N = 24 animals), head direction cells (N = 17 animals), velocity cells (N = 24 animals) and acceleration cells (N = 24 animals) respectively. Bottom: Same as top for anterior-posterior axis. Each dot represents the average per animal per bin along the anterior-posterior axis (left) and along the dorsal-ventral axis. Black lines indicate 95% confidence intervals. *, $p < .05$, **, $p < .01$, Test used in C, linear regression

Figure 1

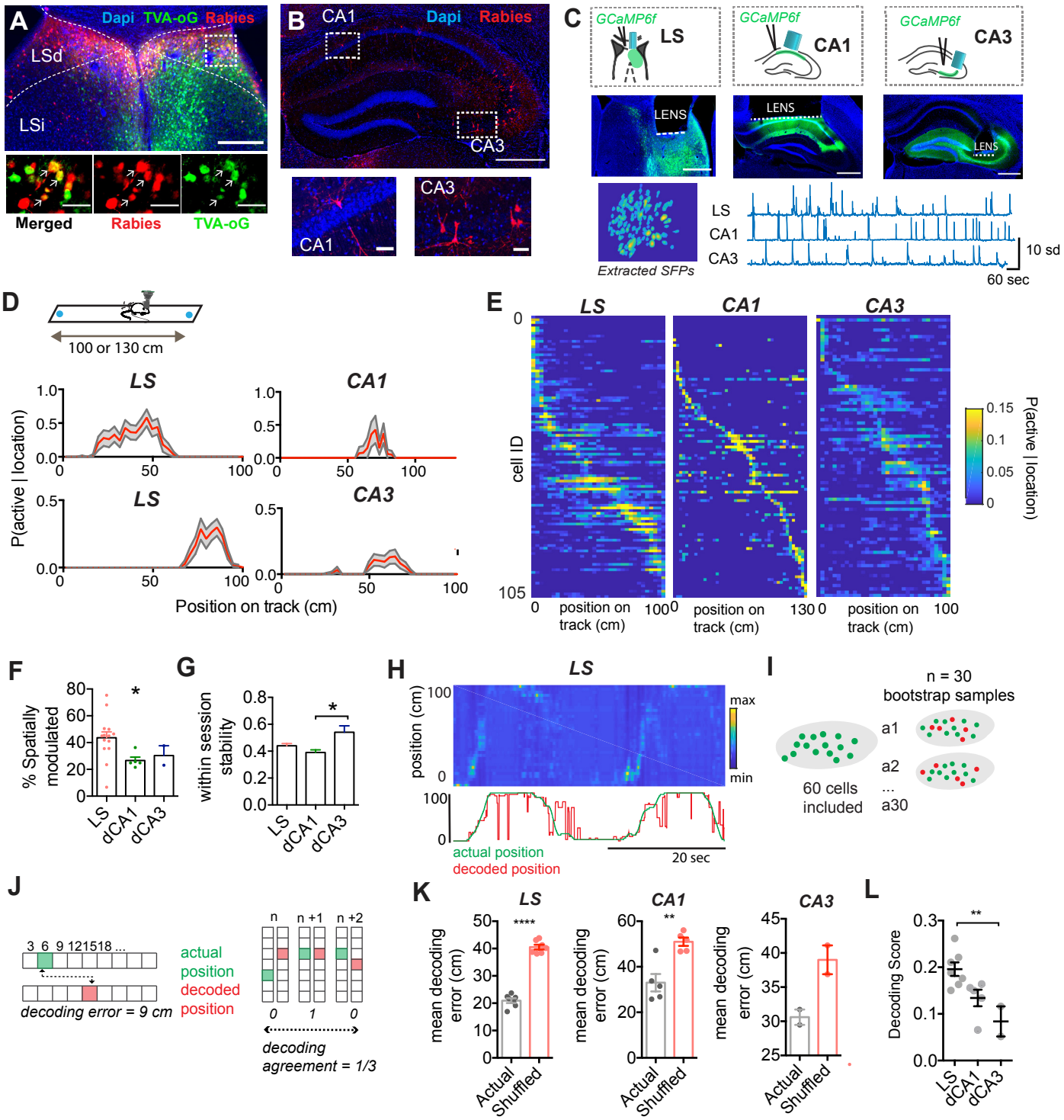
A
Dapi TVA-oG Rabies
LSd
LSi
Merged
Rabies
TVA-oG
B
CA1
Dapi Rabies
CA3
CA1
CA3
C
GCaMP6f
LS
CA1
CA3
LENS
Extracted SFPs
LS
CA1
CA3
10 sd
60 sec
D
100 or 130 cm
LS
CA1
CA3
P(active | location)
Position on track (cm)
E
LS
CA1
CA3
cell ID
position on track (cm)
P(active | location)
F
% Spatially modulated
LS
dCA1
dCA3
G
within session stability
LS
dCA1
dCA3
H
LS
position (cm)
max
min
actual position
decoded position
20 sec
I
n = 30
bootstrap samples
a1
a2
...
a30
60 cells included
J
3 6 9 121518 ...
decoding error = 9 cm
actual position
decoded position
n
n +1
n +2
0
1
0
decoding agreement = 1/3
K
LS
CA1
CA3
mean decoding error (cm)
Actual
Shuffled
L
Decoding Score
LS
dCA1
dCA3

Figure 2

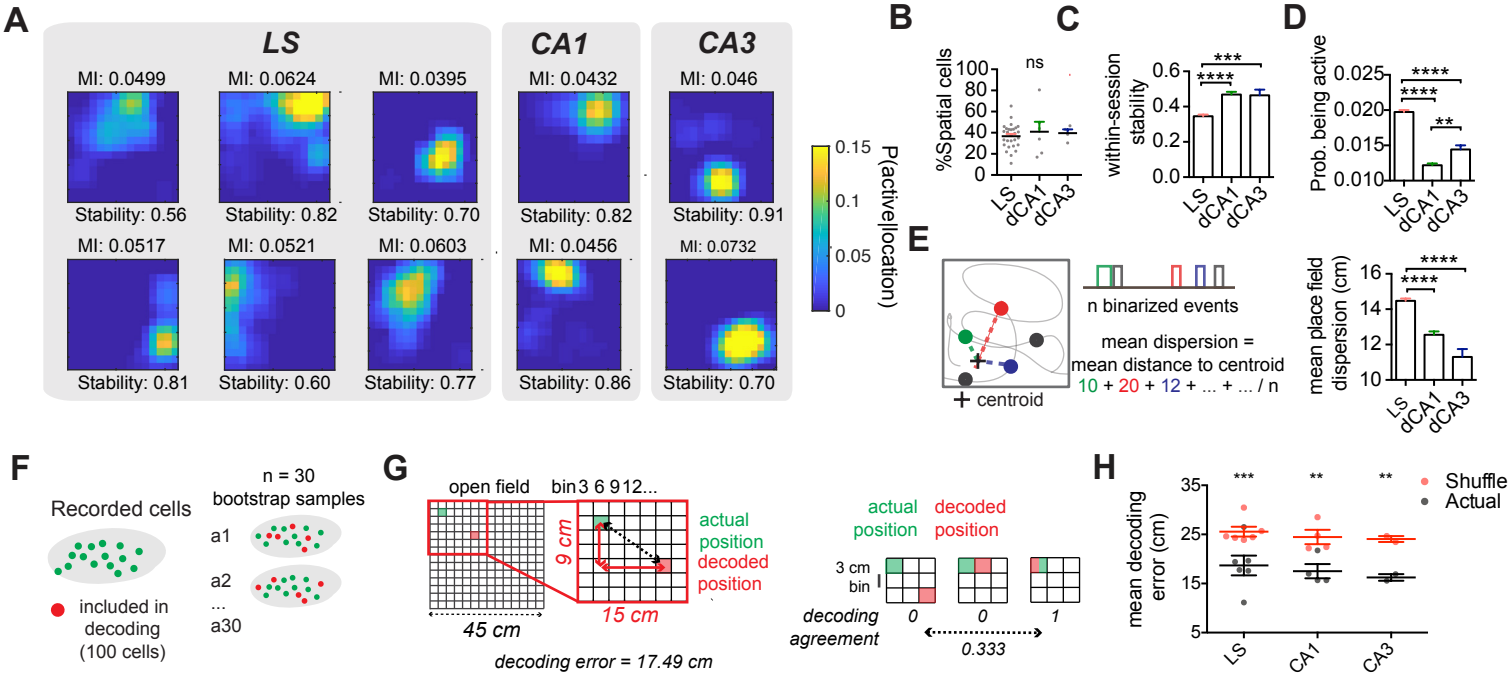
A
LS
CA1
CA3
MI: 0.0499
MI: 0.0624
MI: 0.0395
MI: 0.0432
MI: 0.046
Stability: 0.56
Stability: 0.82
Stability: 0.70
Stability: 0.82
Stability: 0.91
MI: 0.0517
MI: 0.0521
MI: 0.0603
MI: 0.0456
MI: 0.0732
Stability: 0.81
Stability: 0.60
Stability: 0.77
Stability: 0.86
Stability: 0.70
P(active|location)
0.15
0.1
0.05
0
B
%Spatial cells
ns
LS
dCA1
dCA3
C
within-session stability
***
****
D
Prob. being active
****
**
E
n binarized events
mean dispersion =
mean distance to centroid
10 + 20 + 12 + ... + ... / n
centroid
mean place field dispersion (cm)

F
Recorded cells
included in decoding (100 cells)
n = 30
bootstrap samples
a1
a2
...
a30
G
open field
bin 3 6 9 12...
9 cm
15 cm
45 cm
actual position
decoded position
decoding error = 17.49 cm
actual position
decoded position
3 cm bin
decoding agreement
0
0
1
0.333
H
mean decoding error (cm)
Shuffle
Actual
LS
CA1
CA3

Figure 3

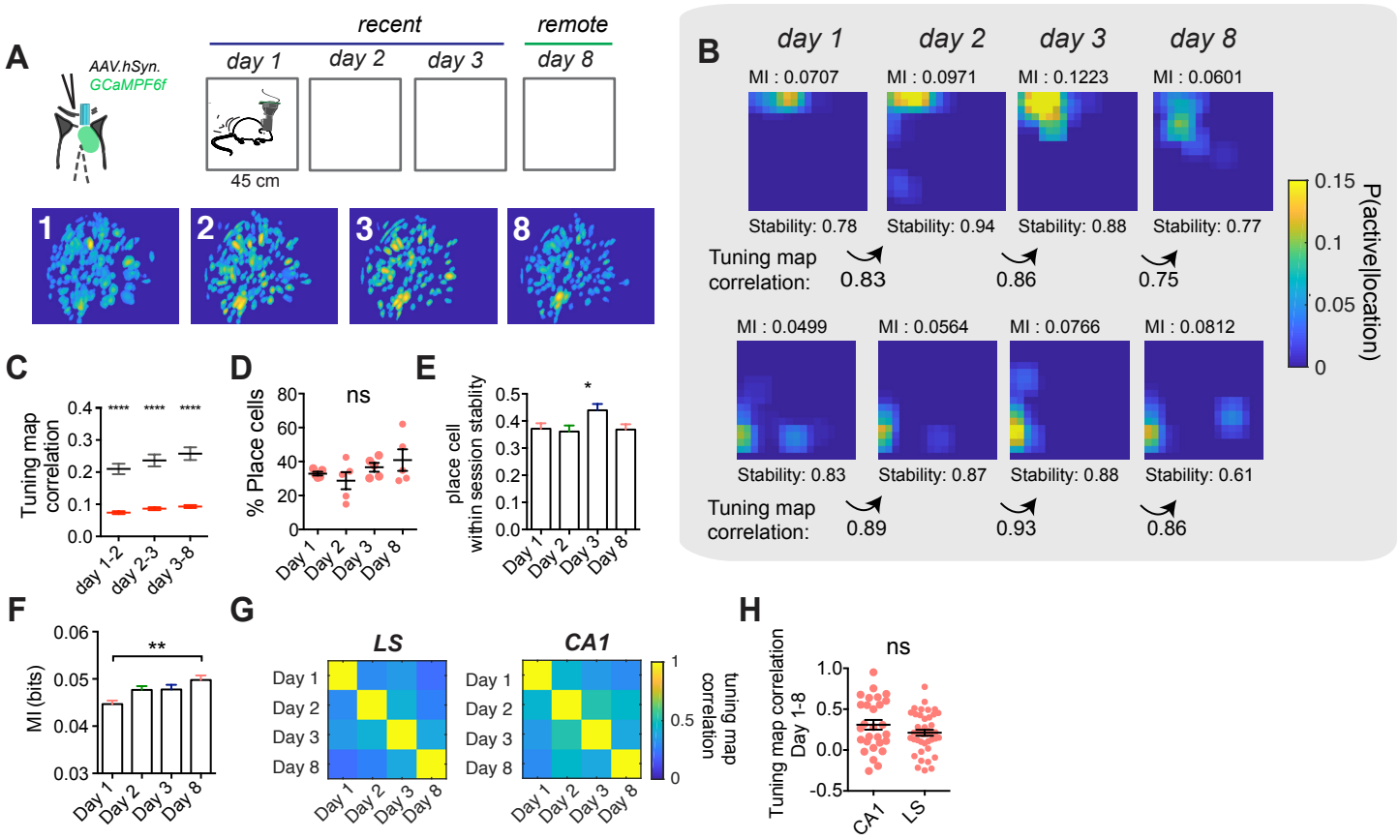
A
AAV.hSyn.
GCaMPF6f
recent
remote
day 1
day 2
day 3
day 8
45 cm
1
2
3
8
B
day 1
day 2
day 3
day 8
MI : 0.0707
MI : 0.0971
MI : 0.1223
MI : 0.0601
Stability: 0.78
Stability: 0.94
Stability: 0.88
Stability: 0.77
Tuning map correlation:
0.83
0.86
0.75
MI : 0.0499
MI : 0.0564
MI : 0.0766
MI : 0.0812
Stability: 0.83
Stability: 0.87
Stability: 0.88
Stability: 0.61
Tuning map correlation:
0.89
0.93
0.86
P(active|location)
0.15
0.1
0.05
0
C
Tuning map correlation
day 1-2
day 2-3
day 3-8
D
% Place cells
ns
Day 1
Day 2
Day 3
Day 8
E
place cell within session stability
Day 1
Day 2
Day 3
Day 8
F
MI (bits)
**
Day 1
Day 2
Day 3
Day 8
G
LS
CA1
Day 1
Day 2
Day 3
Day 8
tuning map correlation
H
Tuning map correlation Day 1-8
ns
CA1
LS

Figure 4

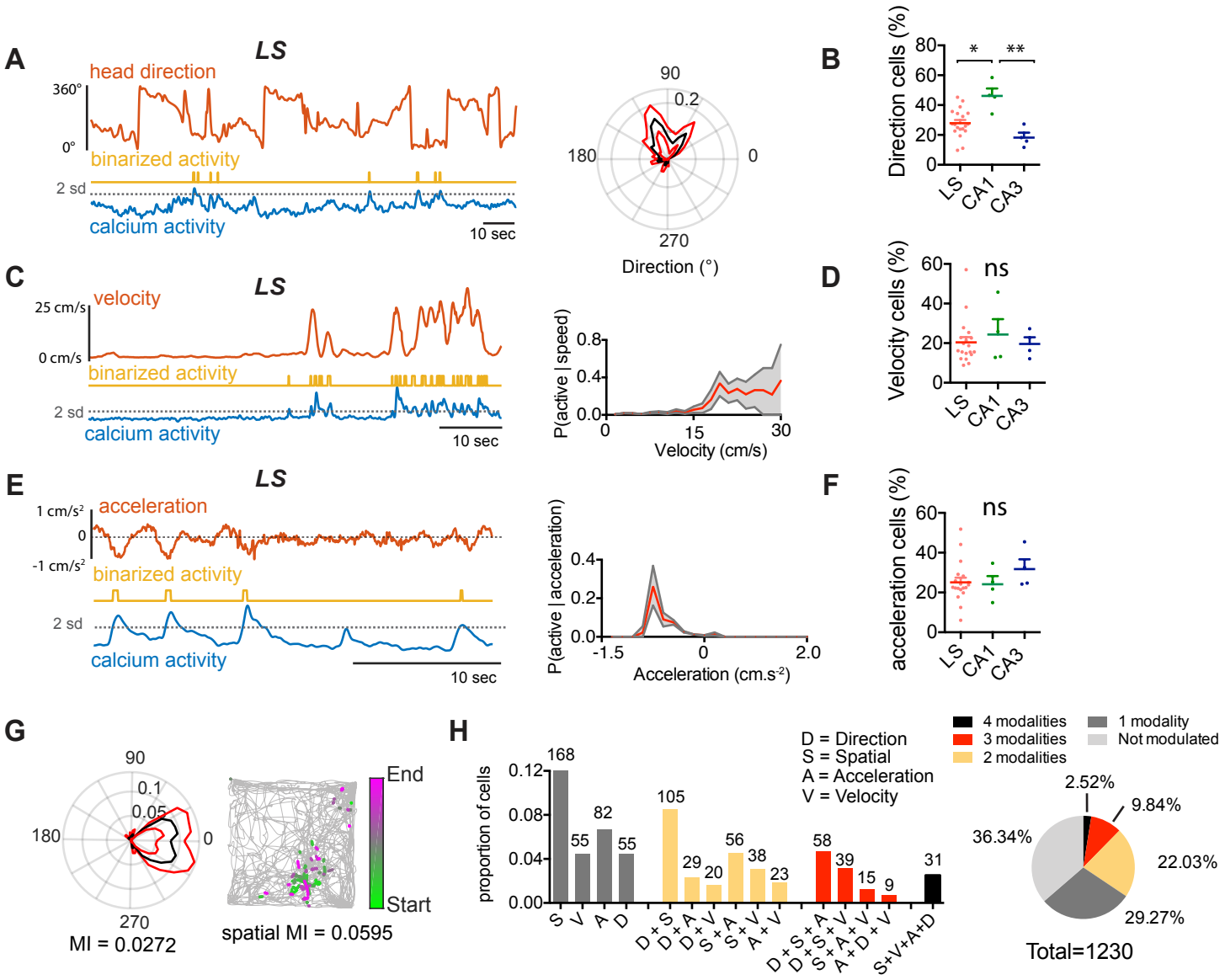
A
LS
head direction
360°
0°
binarized activity
2 sd
calcium activity
10 sec
90
0.2
180
0
270
Direction (°)
B
Direction cells (%)
80
60
40
20
0
*
**
LS
CA1
CA3
C
LS
velocity
25 cm/s
0 cm/s
binarized activity
2 sd
calcium activity
10 sec
P(active | speed)
0.8
0.4
0.0
0
15
30
Velocity (cm/s)
D
Velocity cells (%)
60
40
20
0
ns
LS
CA1
CA3
E
LS
1 cm/s²
acceleration
0
-1 cm/s²
binarized activity
2 sd
calcium activity
10 sec
P(active | acceleration)
0.4
0.2
0.0
-1.5
0
2.0
Acceleration (cm.s-2)
F
acceleration cells (%)
60
40
20
0
ns
LS
CA1
CA3
G
90
0.1
0.05
180
0
270
MI = 0.0272
End
Start
spatial MI = 0.0595
H
D = Direction
S = Spatial
A = Acceleration
V = Velocity
proportion of cells
0.12
0.08
0.04
0.00
168
55
82
55
105
29
20
56
38
23
58
39
15
9
31
S
V
A
D
D + S
D + A
D + V
S + A
S + V
A + V
D + S + A
D + S + V
S + A + V
A + D + V
S+V+A+D
4 modalities
3 modalities
2 modalities
1 modality
Not modulated
2.52%
9.84%
36.34%
22.03%
29.27%
Total=1230

Figure 5

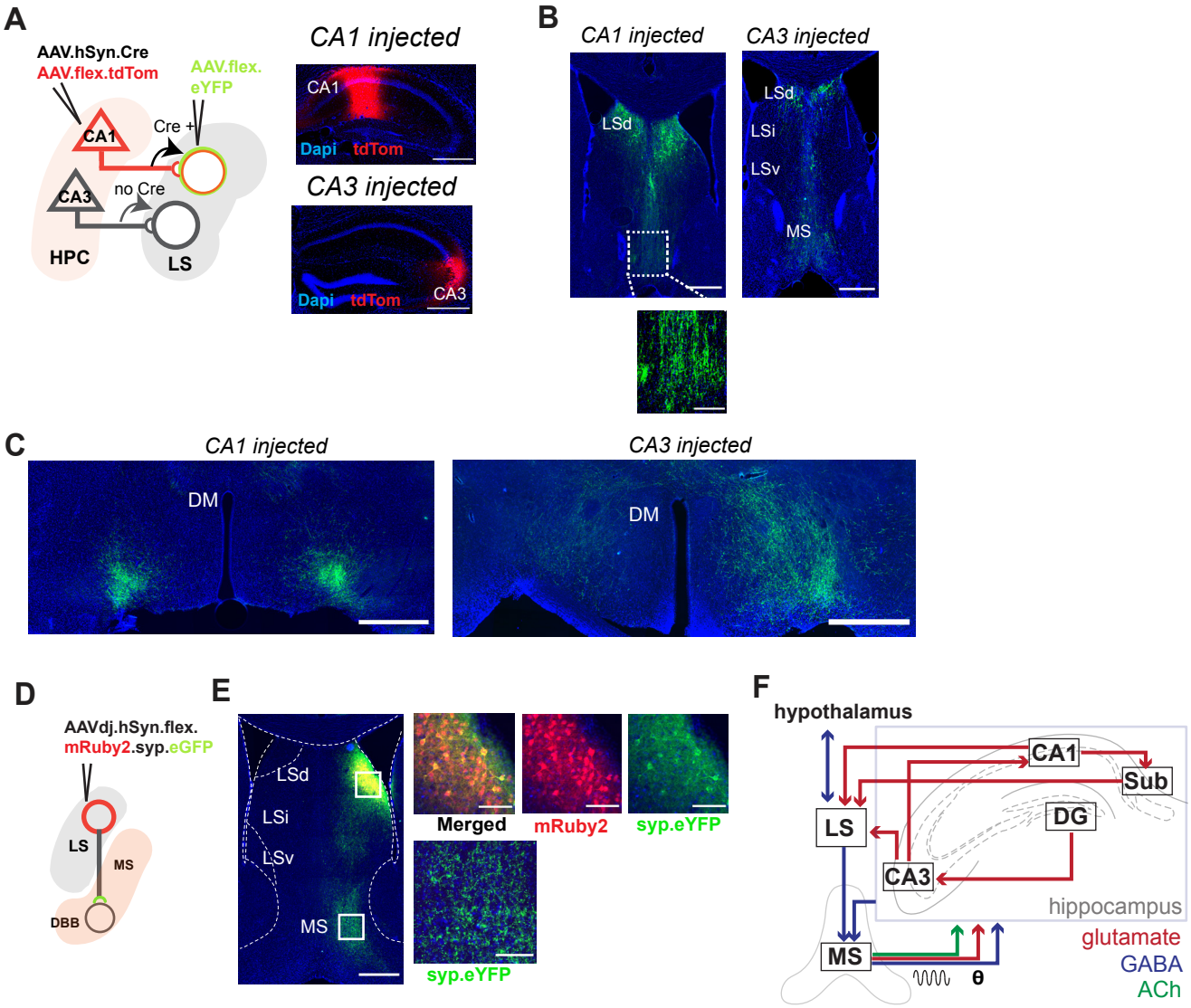
A
AAV.hSyn.Cre
AAV.flex.tdTom
AAV.flex.
eYFP
CA1
Cre +
CA3
no Cre
HPC
LS
CA1 injected
CA1
Dapi
tdTom
CA3 injected
Dapi
tdTom
CA3
B
CA1 injected
CA3 injected
LSd
LSd
LSi
LSv
MS
C
CA1 injected
CA3 injected
DM
DM
D
AAVdj.hSyn.flex.
mRuby2.syp.eGFP
LS
MS
DBB
E
LSd
LSi
LSv
MS
Merged
mRuby2
syp.eYFP
syp.eYFP
F
hypothalamus
CA1
Sub
LS
DG
CA3
hippocampus
MS
θ
glutamate
GABA
ACh

Figure 6

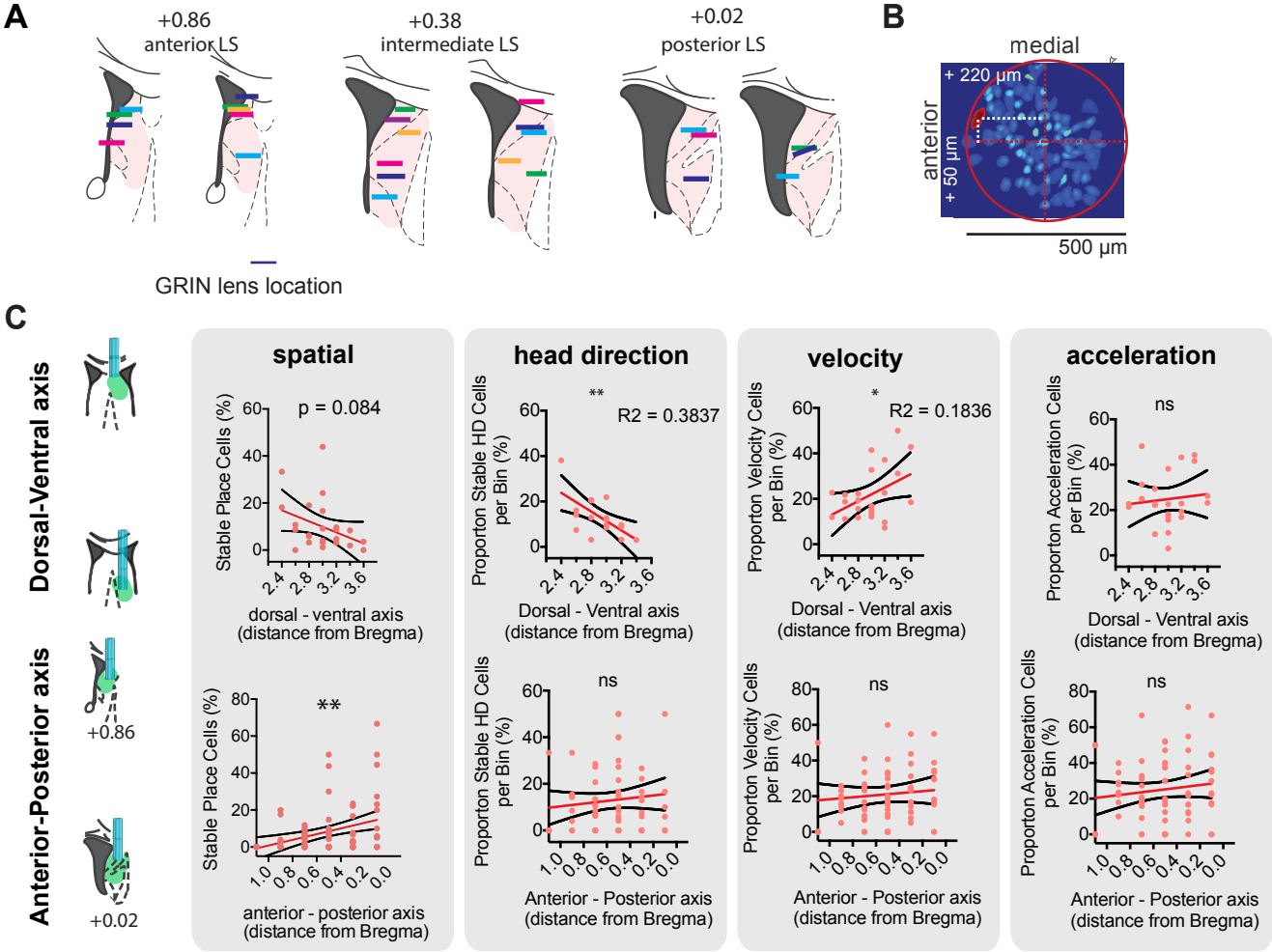
A
+0.86
anterior LS
+0.38
intermediate LS
+0.02
posterior LS
GRIN lens location
B
medial
anterior
+ 220 µm
+ 50 µm
500 µm
C
Dorsal-Ventral axis
Anterior-Posterior axis
+0.86
+0.02
spatial
p = 0.084
Stable Place Cells (%)
dorsal - ventral axis
(distance from Bregma)
**
anterior - posterior axis
(distance from Bregma)
head direction
**
R2 = 0.3837
Proporton Stable HD Cells per Bin (%)
Dorsal - Ventral axis
(distance from Bregma)
ns
Anterior - Posterior axis
(distance from Bregma)
velocity
*
R2 = 0.1836
Proporton Velocity Cells per Bin (%)
Dorsal - Ventral axis
(distance from Bregma)
ns
Anterior - Posterior axis
(distance from Bregma)
acceleration
ns
Proporton Acceleration Cells per Bin (%)
Dorsal - Ventral axis
(distance from Bregma)
ns
Anterior - Posterior axis
(distance from Bregma)